Impact of urban street canyon architecture on local atmospheric pollutant levels and magneto-chemical PM_{10} composition : an experimental study in Antwerp, Belgium

Impact of urban street canyon architecture on local atmospheric pollutant levels and magneto-chemical PM_{10} composition: an experimental study in Antwerp, Belgium

Jelle Hofman[1,2]*, Ana Castanheiro[1]*, Gert Nuyts[3], Steven Joosen[4], Simo Spassov[5], Ronny Blust[4], Karolien De Wael[3], Silvia Lenaerts[6], Roeland Samson[1]

[1]*Laboratory of Environmental and Urban Ecology, Department of Bioscience Engineering, University of Antwerp, Groenenborgerlaan 171, 2020 Antwerp, Belgium*
[2]*Solutions4IoT Lab, Imec, High Tech Campus 31, 5656 AE Eindhoven, The Netherlands*
[3]*Antwerp X-ray Analysis, Electrochemistry & Speciation (AXES), Department of Chemistry, University of Antwerp, Groenenborgerlaan 171, 2020 Antwerp, Belgium*
[4] *Systemic Physiological and Ecotoxicological Research (SPHERE), Department of Biology, University of Antwerp, Groenenborgerlaan 171, 2020 Antwerp, Belgium*
[5]*Division Environmental Magnetism, Department of Geophysics, Royal Meteorological Institute, Dourbes, Belgium*
[6]*Sustainable Energy, Air and Water Technology (DuEL), Department of Bioscience Engineering, University of Antwerp, Groenenborgerlaan 171, 2020 Antwerp, Belgium*

** Equal contribution*

Corresponding author:

Jelle Hofman

Jelle.Hofman@imec.be

Solutions4IoT Lab, Interuniversity Microelectronics Centre (IMEC)

High Tech Campus 31, 5656 AE Eindhoven, The Netherlands

Tel. +(0)32 496 520 240

Key words:

pollution; architecture; natural ventilation; metals; urban; PM composition

Abstract

As real-life experimental data on natural ventilation of atmospheric pollution levels in urban street canyons is still scarce and has proven to be complex, this study, experimentally evaluated the impact of an urban street canyon opening on local atmospheric pollution levels, during a 2-week field campaign in a typical urban street canyon in Antwerp, Belgium. Besides following up on atmospheric particulate matter (PM), ultrafine particles (UFPs) and black carbon (BC) levels, the magneto-chemical PM_{10} composition was quantified to identify contributions of specific elements in enclosed *versus* open street canyon sections. Results indicated no higher overall PM, UFP and BC concentrations at the enclosed site compared to the open site, but significant day-to-day variability between both monitoring locations, depending on the experienced wind conditions. On days with oblique wind regimes (4 out of 14), natural ventilation was observed at the open location while higher element contributions of Ca, Fe, Co, Ni, Cu, Zn and Sr were exhibited at the enclosed location. Magnetic properties correlated with the PM_{10} filter loading, and elemental content of Fe, Cr, Mn and Ti. Magnetic bivariate ratios identified finel-grained magnetite carriers with grain sizes below 0.1 μm, indicating similar magnetic source contributions at both monitoring locations. Our holistic approach, combining atmospheric monitoring with magneto-chemical PM characterisation has shown the complex impact of real-life wind flow regimes, different source contributions and local traffic dynamics on the resulting pollutant concentrations and contribute to a better understanding on the urban ventilation processes of atmospheric pollution.

1. Introduction

To date, road traffic emissions are still a major source of air pollution in urban environments, contributing to atmospheric concentration levels of particulate matter (PM), ultrafine particles (UFPs), nitrogen oxides (NO_x), black carbon (BC). Especially in so-called street canyons, streets with aligned multiple-floor buildings, ventilation and dispersion of local emissions with surrounding and above roof-top air is hindered (Vardoulakis et al., 2003). The magnitude of this street canyon-effect has shown to depend on street architecture (aspect ratio; height vs width; heterogeneity; green infrastructure; openings) (Janhäll, 2015; Kumar et al., 2011; Vardoulakis et al., 2003), wind conditions (Schatzmann et al., 2000) and traffic-induced turbulence (Karra et al., 2011). These effects are yet extensively

studied in laboratory wind tunnel (Ahmad et al., 2005; Buccolieri et al., 2009; Gromke and Ruck, 2007) or numerical model studies (Jeanjean et al., 2017; Morakinyo and Lam, 2016; Nikolova et al., 2011; Pugh et al., 2012; Vos et al., 2013; Vranckx et al., 2015; Wania et al., 2012), but only to a limited extent, and often by using tracers or biological markers, in real-life experimental studies (Goryainova et al., 2016; Hofman et al., 2016a, 2013; Pirjola et al., 2012). Moreover, Karra et al. (2017) recently confirmed the complexity of air flow and air pollution levels in real world heterogeneous street canyons, being much more complex than in simplified homogeneous street canyon models.

Besides the impact on PM concentrations, local street canyon processes might impact the grain size and composition of atmospheric particulate matter (PM) as well. PM consists of a complex mixture of solid and liquid, organic and inorganic, primary and secondary compounds, and is, therefore, highly variable in time and space. Urban anthropogenic PM_{10} is enriched in various trace elements (e.g. metals including Fe, Pb, Zn, Ba, Mn, Cd and Cr), depending on its contributing emission sources (Alves et al., 2018; Hama et al., 2018; Kelly and Fussell, 2012; Keuken et al., 2013; Maenhaut et al., 2016; Mantovani et al., 2018; Sagnotti et al., 2006), and invariably contains magnetic iron oxides and hydroxides (Hansard et al., 2012; Kim et al., 2009; Wang et al., 2017). Urban PM typically consists of 6-18% elemental iron, of which magnetic iron oxides and hydroxides comprise 10-70% (Dedik et al., 1992; Weber et al., 2000), allowing for magnetic quantification and characterization of urban dusts in pumped-air filters, soils, sediments, biological and artificial substrates and human tissues (Evans and Heller, 2003; Hofman et al., 2017; Ma et al., 2015; Maher et al., 2016; Matzka and Maher, 1999; Muxworthy et al., 2003; Oldfield and Scoullos, 1984; Rai, 2013; Sant'Ovaia et al., 2015; Thompson and Oldfield, 1986; Wang et al., 2017; Yang et al., 2010). Moreover, magnetic differentiation between industrial, traffic and natural sources, based on magnetite:hematite ratios (Hansard et al., 2012, 2011) and coercivity distributions (Lu et al., 2016; Magiera et al., 2011; Sagnotti et al., 2006; Spassov et al., 2004; Wang et al., 2017; Zhang et al., 2012), has been demonstrated in earlier studies. Magnetic characterization, therefore, presents a complementary source of air pollution information, e.g. together with atmospheric pollutant concentrations and trace elemental composition, and helps in understanding the source, fate and distribution of environmental contaminants. Enclosed street canyons might for example favor accumulation of street dust (Alves et al., 2018; Wang et al., 2012;

Zhang et al., 2012), when compared to more open sections or junctions. This might result in higher local contributions of resuspended street dust from e.g. non exhaust particles, brake and tire wear or pavement abrasion (Amato et al., 2009; Harrison et al., 2012; Sanderson et al., 2016).

As real-life experimental data on architectural street canyon effects on local atmospheric pollution levels is still scarce and has proven to be complex, this study, experimentally evaluated the impact of urban street canyon openings on local atmospheric pollution level, composition and grain size, during a 2-week (August 16-31, 2017) field campaign in a typical urban street canyon in Antwerp, Belgium. Besides following up on atmospheric PM, UFP and BC levels, the magneto-chemical PM_{10} composition was quantified as well to identify contributions of e.g. street dust resuspension in enclosed street canyon sections. Based on the current literature data from simplified theoretical street canyon models, we hypothesize (i) higher overall atmospheric pollutant levels for PM, UFP and BC, and (ii) a higher contribution from street dust elements, at the enclosed street canyon section (E) when compared to the open street canyon section (O).

2. Material & Methods

2.1 Study site

The considered street canyon (Markgravelei) is located within a medium-trafficked residential area in the densely populated city center of Antwerp (2582 inhabitants km^{-1}), Belgium. It is oriented perpendicular to the prevailing southwesterly wind direction, consists of two opposing traffic lanes and has a typical street canyon geometry with a height (H) of 10-12 m, length (L) of 650 m and a width (W) of 14 m. According to the geometry rules described by Vardoulakis et al. (2003), the street canyon can thus be described as a symmetric long (L/H > 7) regular street canyon (aspect ratio (H/W) < 1). Two monitoring locations within this street canyon, ~260 m apart, were considered; the “enclosed” location (E) consisting of 3-4 story buildings alongside bothstreet facades, while the “open” location (O) was characterized by 3-4 story buildingfacade along one side, and an urban park (Hof van Leysen) along the other side of the street canyon (Figure 1). This implies that the ventilation and dilution properties of roadside emissions will be impaired near the enclosed (E) location, typically referred to as the street canyon effect (Gromke and Ruck, 2012; Janhäll, 2015; Kumar et al., 2011; Nicholson, 1975; Vardoulakis et al., 2003; Wania et al., 2012), while the open (O) location will allow for more ventilation with surrounding air due to the porous urban green patch. The considered street

is surrounded by similar street configurations (3-4 story residential buildings) at the north, east and west, and an adjacent urban park with more distant (~600 m) ring road at the south-west (Figure 1 and appended kmz files).

Figure 1: Location of the considered street canyon locations (E, O) and regulatory monitoring stations (R801, R802, R817) in Antwerp with streetview images of the enclosed (E; top left; 51°12'2.05'' 4°23'55.37'') and open (O; bottom right; 51°11'56.58'' 4°24'5.80'') sampling locations (see supplementary KMZ files as well; source: © 2018 Google).

2.2 Monitoring equipment

2.2.1 Gravimetric PM_{10} sampling

At both monitoring locations (E and O), cumulative 24-hour air-pumped PM_{10} samples were collected on quartz membrane filters (Tissuquartz 2500 QAT-UP) at inhalation height (~1.5 m) and flow rate of 2.3 m^3 h^{-1} (55.2 m^3 day^{-1}) for two weeks, between August 17th and 30th, 2017, using a low-volume Leckel SEQ 47/50 (Leckel, Germany) gravimetric sampler at each of the considered locations (E and O; Figure 2). The sampling flow of the Leckels was calibrated in the field, using a BGI DeltaCal air flow calibrator (Mesalabs, US), and checked (max 5% deviation; 36.41-40.25 lpm) during each of the

consecutive point measurement campaigns (see 2.2.3). After 24-hour sampling, PM_{10}-loaded filters were stored automatically in covered filter cartridges (to avoid volatile compound losses) inside the Leckel SEQ 47/50, before being transported to the laboratory. The instrument status; i.e. flow rate (m^3 h^{-1}), sampling time, sampled volume (m^3), ambient and internal atmospheric temperature (°C) and pressure (mbar) were was consulted daily using the supplied StatusView software (Leckel, v2.45).

2.2.2 Meteorological data

Meteorological data on atmospheric temperature (°C), wind speed (m s^{-1}) and wind direction (°), was collected from the nearest (2.25 km) available regulatory monitoring station (R802) of the Flanders Environment Agency, at an hourly resolution.. Wind direction and speed will namely largely influence the ventilation properties of street canyons, e.g. perpendicular vs parallel wind flow (Gromke and Ruck, 2012; Kumar et al., 2011; Ng and Chau, 2014; Vardoulakis et al., 2003). Ambient atmospheric temperature (°C) and pressure (mbar) inside the street canyon were quantified automatically by the SEQ 47/50 samplers.

2.2.3 Point measurements of PM_{10}, BC and UFP

At both street canyon locations (E and O), 10 second-averaged atmospheric measurements of PM_{10}, BC and UFP were collected for 30 minutes with wearable instruments on August 17th, 22nd, 25th, 28th and 30th, 2017, resulting in 2.5 hours of total monitoring data per pollutant per location. Measurements were performed alternately, in 15-minute intervals (O1 – E1 – O2 – E2), during morning and evening rush hours (8-10h and 16-18h) and afternoon hours (13-16h). During the point measurement campaigns, simultaneous manual traffic counts were performed of all passing motorised road traffic (passenger and heavy-duty traffic).

Atmospheric PM_{10} concentrations were measured with a Dusttrak™ II (TSI, USA) equipped with a particle size cut-off impactor (10 µm). UFP measurements were collected using a P-Trak® Ultrafine Particle Counter (Model 8525, TSI, USA), quantifying fine-grained particles with aerodynamic diameters between 0.02 and 1 µm, by condensational growing of particles (using isopropyl alcohol) and subsequent optical particle counting. The P-Trak has a flow rate of 700 ml min^{-1} and the monitoring resolution was set to 10 second intervals.

The atmospheric concentration of optically absorbing aerosol particles (equivalent black carbon, ng m^{-3}) was determined using a AE51 microaethalometer (Aethlabs, USA), from the changing light attenuation (at 880 nm) of a particle spot on an air-pumped T60 Teflon-coated borosilicate glass filter. More information on the underlying measurement principle and applied noise (ONA) and filter loading corrections can be found in Appendix 1.

Figure 2: Left: On-site fencing, meteorological mast and monitoring equipment for the continuous gravimetric PM_{10} measurements (Leckel SEQ 47/50). Right: Applied portable PM_{10} (TSI Dusttrak II), UFP (TSI P-Trak) and BC (Aethlabs AE51 microaethalometer) instruments for the point measurement campaigns.

2.3 Laboratory analyses

2.3.1 Gravimetric PM_{10} sampling

Following the European EN12341 standard for gravimetric PM_{10} sampling, the quartz fibre filters (E17-E30 and O17-O30) were pre-weighed after a preconditioning period of >48 hours (August 3-16, 2017) in a climatised weighing room at a relative humidity of 50%, using a MT5 microbalance (Mettler-Toledo Ltd., Austria) with 1 µg sensitivity. A second pre-weighing was conducted after another conditioning period >12 hours (weight difference ≤40 µg). Subsequently, pre-weighed filters were loaded in filter cartridges, together with a procedure blank, and loaded in the Leckel SEQ 47/50 samplers. After sampling, the full filter cartridges were transported to the laboratory, conditioned for >48 hours and post-weighed. A second post-weighing was conducted in a 24-72 hour time window,

provided that the post-weighing difference did not exceed 60 µg. Otherwise, another conditioning period of 24 hours was required following a third post-weighing. The average filter loading (µg) was subsequently divided by the sampled volume of air (m^3) to obtain the average daily atmospheric PM_{10} concentration (µg m^{-3}). After quantifying the filter loading, the filters were analysed for their trace element concentrations using ED-XRF (2.3.3). Subsequently, filters were cut in half and one filter half was used for magnetic analysis (2.3.2), while the other half was used for HR-ICP-MS analysis (2.3.3).

2.3.2 Magnetic PM_{10} analysis

The filter-loaded PM_{10} samples (half filters) were analysed for a range of magnetic properties in order to evaluate their PM_{10} magnetic concentration, mineralogy, domain state and grain size (Evans and Heller, 2003; Hofman et al., 2017; Maher et al., 1999). Bulk low-frequency magnetic susceptibility (χ_{LF}; SI) under 200 and 450 A m^{-1} bias fields was determined at the laboratories of Magnetic Valley (magneticvalley.be; Dourbes, Belgium), with a highly sensitive ($2x10^{-8}$ SI) Kly-4 Kappabridge (AGICO Inc., CZ), as the MS2B Magnetic Susceptibility System (Bartington Ltd., England) sensitivity ($2x10^{-6}$ SI) proved to be insufficient for our PM_{10}-loaded filter samples. Subsequently, all PM_{10} filters were transported to the magnetic lab of the Bioengineering Department at the University of Antwerp, Belgium, and consecutively analysed for their *Anhysteretic Remanent Magnetisation* under 200 AC field and 500 bias DC field ($ARM_{200/500}$; A m^{-1}), *Saturation Isothermal Remanent Magnetisation* (SIRM; A m^2 kg^{-1}) and 300mT backfield magnetisation (IRM_{-300}; A m^2 kg^{-1}). From these magnetic properties, additional magnetic indicators S-ratio ($SIRM/IRM_{-300}$), HIRM ($0.5\times(SIRM+IRM_{-300})$), SIRM/$\chi_{LF}$ and ARM/SIRM were calculated, providing information on the relative contribution of high- to low-coercivity magnetic compounds and magnetic grain size (Evans and Heller, 2003; Hofman et al., 2017; Maher et al., 1999). While SIRM and ARM exhibit grain size dependence, χ_{LF} is size-independent. As a result, high SIRM/X_{LF} and ARM/SIRM ratios point to high contributions of smaller-grained single domain (SD) or pseudo-single domain (PSD) magnetite particles (Hofman et al., 2017). The ARM susceptibility, ARMχ, is defined as the ARM magnetization, normalized by the net weight of filter-collected PM, divided by the bias DC field used to give the ARM; the SI unit is m^3 kg^{-1}.

2.3.3 Elemental PM_{10} composition

Different analytical techniques exist for chemical and physical characterisation of PM (Galvão et al., 2018). As our study aimed at quantifying trace elements (e.g. heavy metals) in collected PM samples, requiring low detection limits, and representative analytical techniques (for comparison with regulatory EU data), we opted for two different analytical techniques, using atomic spectrometry (HR-ICP-MS; destructive) and X-ray (ED-XRF; non-destructive) principles (Galvão et al., 2018).

Firstly, the full PM-loaded filters were analysed for 17 elements; Mg, Al, Si, K, Ca, Ti, V, Cr, Mn, Fe, Co, Ni, Cu, Zn, Rb, Sr, Pb with ED-XRF (energy dispersive X-ray fluorescence), using the Epsilon5 (PANalytical) which has a Gd anode tube (600 W maximum power) and is equipped with several secondary targets. For the analyses of Na-Sc and Ru-Sn in the samples the following parameters were used: tube voltage of 25kV, current of 24mA, live time of 500s and a Ti secondary target. Ti-Ga and Sb-Er: 75kV, 8mA, 1000s and Ge secondary target. Ge-Nb and Tm:Bi: 100kV, 6mA, 1000s and Mo secondary target. The same parameters were used for the analyses of the blanks, but with twice the lifetime. Two procedure blanks (B1-B2) were used together with four regular blank filters. Spectra were fitted using baxil (Brightspec) and compared to all the blank measurements. Quantification was performed by using sensitivity coefficients which were determined by measuring thin reference films and using a thin film approximation allowing the concentration (ng cm^{-2}) to be determined.

Subsequently, filters were cut in half and HR-ICP-MS (high-resolution inductively coupled plasma mass spectrometry) was applied on one filter half by transferring it to a polypropylene tube. To extract the metals, 0.125 ml concentrated HNO_3 (TraceMetal Grade, Fisher Chemical) was added and subsequently heated for 60 minutes at 115°C using a heating block (HotBlock, Environmental Express). After dilution to 4 ml, all samples were analysed using HR-ICP-MS (ELEMENT 2, Thermo Scientific) for 27 elements; Na, K, Rb, Mg, Ca, Sr, Ti, V, Cr, Mo, Mn, Fe, Co, Rh, Ni, Pd, Cu, Ag, Zn, Cd, Al, Tl, Si, Pb, As, Sb, U. The obtained element concentrations (µg l^{-1}) corrected for the procedure blank concentrations. normalised to the applied analytical volume and recalculated to atmospheric element concentrations (ng m^{-3}), using the volume of sampled air (m^3) and doubled to obtain full-filter concentrations (for reference against ED-XRF results). For elements that fell below the limit of

detection (BMQL), normalisation and recalculations were conducted with half the limit of detection (MQL=0.001 µg l^{-1}), following Custer et al. (2000).

2.4 Statistical analysis

Normality was evaluated visually (qqplot and histograms) and from Shapiro-Wilk normality tests. One-way ANOVA and non-parametric Wilcoxon / Kruskal-Wallis Tests (Rank Sums) were applied to test whether the obtained gravimetric and point measurements for PM_{10}, UFP and BC differed between the considered locations (E, O). Where applicable, Pearson and Spearman Rank (non-parametric) correlation tests were applied to evaluate associations between different variables. Multivariate linear regression models were applied to test the influence of multiple variables. Analyses were conducted in the JMP Pro v14.0.00 (SAS Institute Inc., 2018) and RStudio v1.1.383 (RStudio Inc., 2017).

3. Results & Discussion

3.1 Gravimetric PM_{10} sampling

The obtained 24-hour PM_{10} loading on the filters (Figure 3) varied from 438 µg to 2.24 mg, resulting in atmospheric particle concentrations of 7.94 µg m^{-3} and 40.69 µg m^{-3}, when normalised for the sampled volume of air (55.13 - 55.16 m^3). Atmospheric PM_{10} concentrations within the street canyon seem to increase throughout the considered monitoring period (August 17-31) at both locations (E and O; bars in Figure 3) and show good agreement with the nearest regulatory monitoring stations (urban background in city centre (R801), roadside city centre (R802) and urban background outside city centre (R817)) of the Flanders Environment Agency (VMM) (lines in Figure 3). Spearman Rank correlations confirm the observed agreement between our street canyon data (µg m^{-3}) and regulatory stations R801 ($r = 0.97$, $p < 0.0001$, $n = 28$), R802 ($r = 0.97$, $p < 0.0001$, $n = 28$) and R817 ($r = 0.94$, $p < 0.0001$, $n = 26$), with *Root Mean Squared Errors* (RMSE) of, respectively, 4.4, 4.9 and 3.7 µg m^{-3}. One-year averaged and median data (for 2017) from a nearby regulatory station (M802) were similar (respectively 24 and 20 µg m^{-3}) to the exhibited concentrations in our short-term monitoring campaign.

3.2 Effect of street architecture and metorology

For 10 out of 14 sampling days, the earlier-described reduced ventilation hypothesis (i) at the enclosed street canyon location seems to be confirmed with on average 11% higher PM_{10} concentrations, when compared to the open street canyon location. However, for four days the PM_{10} concentration is on average 19% lower at the enclosed monitoring location. On average, a modest difference of about 3% is observed between the enclosed and open monitoring location (22.36 vs 22.14 µg m^{-3}) and one-way ANOVA testing indicates no significant difference between the enclosed and open monitoring locations (F ratio = 0.0043, p = 0.95), while significant day-to-day differences (F ratio = 23.75, p < 0.0001) are observed.

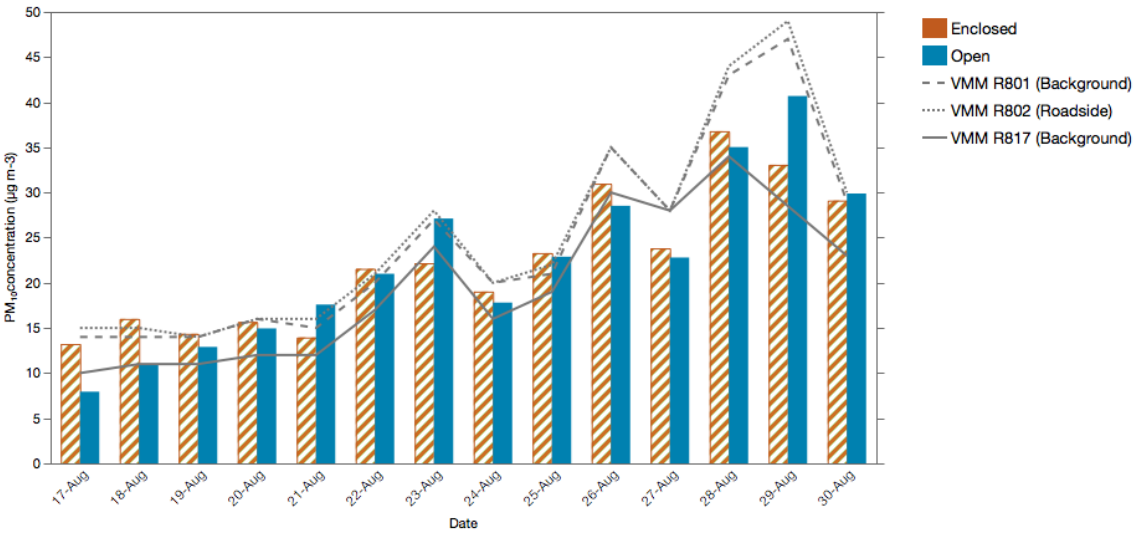

Figure 3: Obtained daily PM_{10} mass concentrations (µg m^{-3}) at the enclosed (striped bars) and open (blue bars) street canyon locations, compared to reported PM_{10} concentrations from the nearest regulatory urban background (R801; stacked line) and roadside (R802; dotted line) stations, and suburban background (R817; full line) station.

As the observed PM_{10} concentration differences between the enclosed (E) and open (O) monitoring locations were not consistent but showed day-to-day variability,we had a closer look at the meteorological conditions experienced during our sampling campaign.

Considering the effect of wind regimes (oblique vs parallel) on natural ventilation of urban street canyons, we compared the daily -averaged PM_{10} loadings with the daily (vector)-averaged wind regimes (Appendix 3). Doing so, higher PM loadings at the open location (August 21, 23, 29 and 30), seemed to coincide with parallel wind directions, either south-easterly (141-187°) or north-westerly (336°),while on days with overall oblique wind flow (225 - 270°; August 18, 19, 20 and 24) higher

PM_{10} loadings were exhibited at the enclosed location. The observed influence during parallel wind conditions seems to suggest local PM_{10} source contributions, possibly from nearby façade renovation works (conducted at 100m and 360m from, respectively, the open and enclosed monitoring locations) or nearby busy traffic intersections, while the impaired natural ventilation (hypothesis i) of the street canyon, seem to be confirmed during oblique wind conditions. Nevertheless, this study points out that due to the varying nature of wind speed and direction, these favourable wind conditions facilitating natural ventilation at the open location only represent 4 out of 14 days.

Ambient temperature readings monitored by the Leckel SEQ47/50 samplers (within the street canyon) correlated nicely with the nearest regulatory ambient temperature readings for both the enclosed (R^2 = 0.94; n= 14) and open (R^2 = 0.90; n = 14) street canyon location, and was, respectively 1.91 and 1.80 °C higher, when 14-day averages were compared to the regulatory data. The ambient temperature readings were very similar between both monitoring locations (R^2 of respectively >0.99 and 0.98), and representative when compared to the campaign-averaged (19°C), but higher than the yearly-averaged temperature (12 °C) for 2017 derived from a nearby regulatory station (M802). From multiple linear regression models, we learn that the contributing effects of temperature ($p < 0.0001$) and wind speed ($p < 0.001$) on measured PM_{10} concentrations, exhibit significant interactions mutually ($p < 0.001$) and with wind direction ($p < 0.01$), explained by the fact that higher wind speeds (>3 m s^{-1}) seem to be associated with south-westerly (SW) wind directions (200 - 250°; Figure 5), resulting in atmospheric temperature decreases (16 - 19 °C), when compared to days with lower wind speeds (20 - 24°C). From the pollution rose in Figure 4, it becomes clear that lower wind speeds result in higher PM_{10} concentrations, indicating local PM_{10} source contributions (i.e. road traffic). Nevertheless, when the wind direction is coming from the NW, slightly increased PM_{10} concentrations are observed, probably linked to the upwind presence of traffic intensive intersections (*Brederodestraat – Montignystraat – Amerikalei – Singel*).

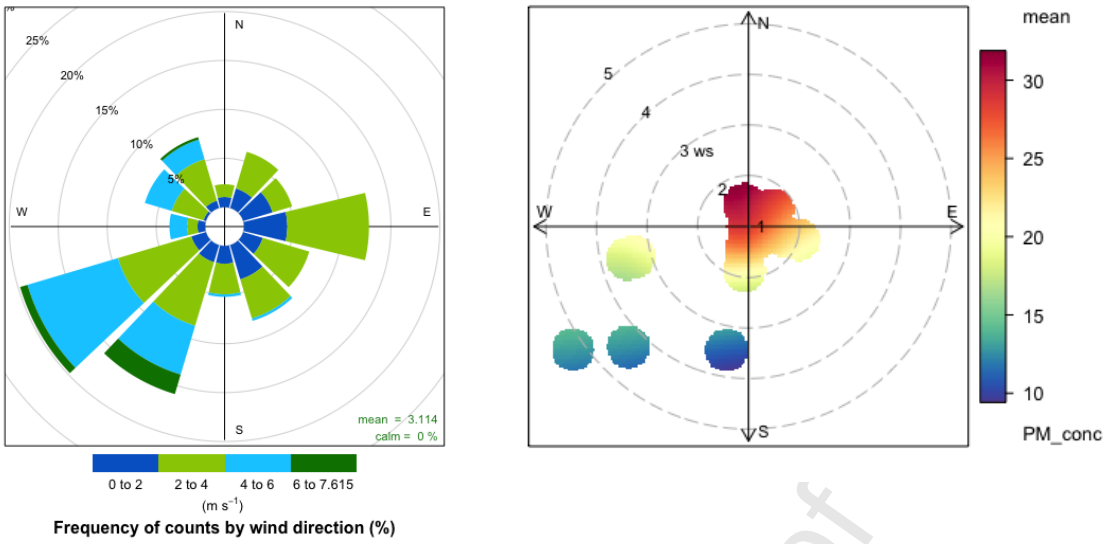

Figure 4: Windrose plot based on hourly measurements during the field campaign (August 17th- 30th, 2017) representing wind speed (m s^{-1}) and direction (°) at the nearest regulatory monitoring station (left) and resulting pollution rose based on daily-averaged local PM_{10} concentrations (PM_conc; ug m^{-3}) within the considered street canyon (right).

From correlation matrices between gravimetric, meteorological and magnetic variables (Figure 5), the observed dust loading on the filters (and therefore atmospheric PM_{10} concentration) seems to be positively associated with atmospheric temperature (r = 0.82), regulatory PM_{10} data (r = 0.95), concentration-dependent magnetic parameters (raw SIRM and susceptibility X; r = 0.63-0.66), and negatively associated with wind speed (r = -0.78) and HIRM (r = -0.7). Hierarchical clustering identifies clusters between (i) HIRM and wind flow; (ii) magnetic properties SIRM, X and S-ratio; and (iii) PM_{10} load, regulatory PM_{10} concentration and temperature (Figure 5). When evaluating these effects at the individual sampling locations (enclosed vs open; Appendix 5), stronger associations with magnetic properties (r = 0.68-73) and weaker meteorological effects due to temperature (r = 0.79) and wind speed (r = -0.76) are exhibited at the enclosed location, when compared to the open street canyon location (respectively r = 0.56-0.58, r = 0.85 and r = -0.81). While for the enclosed street canyon location, the stronger magnetic response suggests a higher magnetic composition of the dust (see 3.3), possibly due to the inhibited street canyon ventilation, and therefore higher contribution of locally-emitted metallic road traffic emissions (see 3.3).

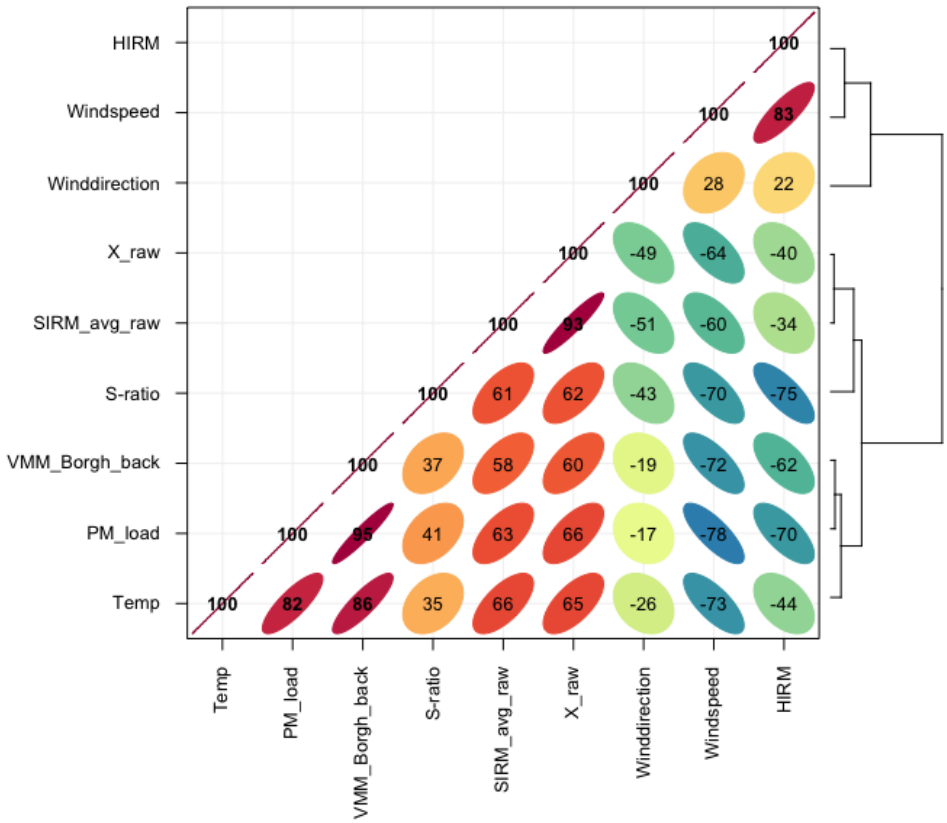

Figure 5: Correlation matrix showing associations between atmospheric temperature (Temp; °C), filter loading (PM_load; ng), atmospheric PM_{10} concentration at a regulatory urban background station (VMM_Borgh_back; ug m^{-3}), S-ratio, average raw SIRM (SIRM_avg_raw; A m-1), raw susceptibility (X_raw;), Wind direction (Winddirection; °), Windspeed (Windspeed; m s-1) and HIRM (HIRM;). The degree of (positive) association is denoted by colour, density ellipses and correlation coefficients, while the data is hierarchically clustered (dendrogram right hand side).

3.3 Elemental PM_{10} composition

From the ED-XRF and HR-ICP-MS analyses of the PM-loaded filter samples (ng), daily-averaged atmospheric (ng m^{-3}) and mass concentrations (µg g^{-1}) were calculated, ranging from 1.17 to 1515.58 ng m^{-3} (ED-XRF; Appendix 3) and 0.0004 to 1630.03 ng m^{-3} (HR-ICP-MS; Appendix 4), while mass concentrations ranged from 2.11 µg g^{-1} to 85.0 mg g^{-1} and 29.5 µg g^{-1} to 85.4 mg g^{-1} (Appendix 5 and 6). When comparing element concentrations between the considered analytical techniques (ED-XRF vs HR-ICP-MS), similar element concentrations were obtained for K, Ca, Mn, Fe, Ni, Cu, Zn, Sr and Pb, while more distinct concentrations for Co, Cr, Rb, Si and Ti were observed. From an analytical

point of view, the high Si contribution in our ED-XRF results can be explained by the filter media (Pall Tissuquartz™, 2500 QAT-UP), made out of pure quartz (SiO_4), contributing to large, broad Si spectrum peaks covering the Al and Mg peaks as well making these filters unsuitable to quantify Si, Al and Mg by ED-XRF. For the common elements (17), similar profiles are observed when comparing both methodologies (ED-XRF vs HR-ICP-MS; Appendix 7), and considered monitoring locations in Figure 6 (enclosed vs open). Ca, Fe and K appear to be the governing elements, while Pb, Cu and Zn are notable as well. None of the governing (yearly averaged) limit values for Pb (500 ng m^{-3}; EU) and Cd (30 ng m^{-3}; VLAREM II) or target values for As (6 ng m^{-3}; EU), Cd (5 ng m^{-3}; EU), Ni (20 ng $m^{-}3$; EU) and Mn (150 ng m^{-3}; WHO) were exceeded during the considered monitoring period. The elemental PM_{10} composition (Figure 6) observed at both monitoring locations (E and O) indicates similar dominant source contributions at both sites. This seems logical, as both monitoring sites were only located 260 m apart within the same street canyon. To evaluate potential street architecture effects on pollutant concentrations, equal source contribution and strength at both monitoring locations are important constraints. Besides the similar elemental composition at both monitoring locations, multiple linear regression analysis indicates higher element concentrations ($p = 0.005$) at the enclosed monitoring location, when compared tothe open location. Moreover, this location effect seems to be element-specific (interaction effect; $p<0.0001$), most profoundly observed for Ca and Fe, followed by Co, Ni, Cu, Zn and Sr (Figure 6). Alves et al. (2018) observed high enrichment factors for Pb, Zn, Fe, Cu, Sn and Sb in street dust collected in Portugal. In Belgium, Maenhaut et al. (2016) attributed Cu, Fe, Mo and Sb to traffic, Al, Ba and Zn to non-exhaust traffic and Ca, Al, Mn, Ti to crustal matter sources (local contributors to urban street dust), while Moretti et al. (2018) observed elevated levels of Fe (874 and 1692 ng m^{-3}), Cr (3.4 and 7.7 ng m^{-3}), Zn (59.1 and 71.2 ng m^{-3}) and Cu (41.1 and 48.4 ng m^{-3}) at two roadside locations (n = 17), compared to two urban green (n = 12) and two industrial (n = 15) sites in Antwerp, Belgium.

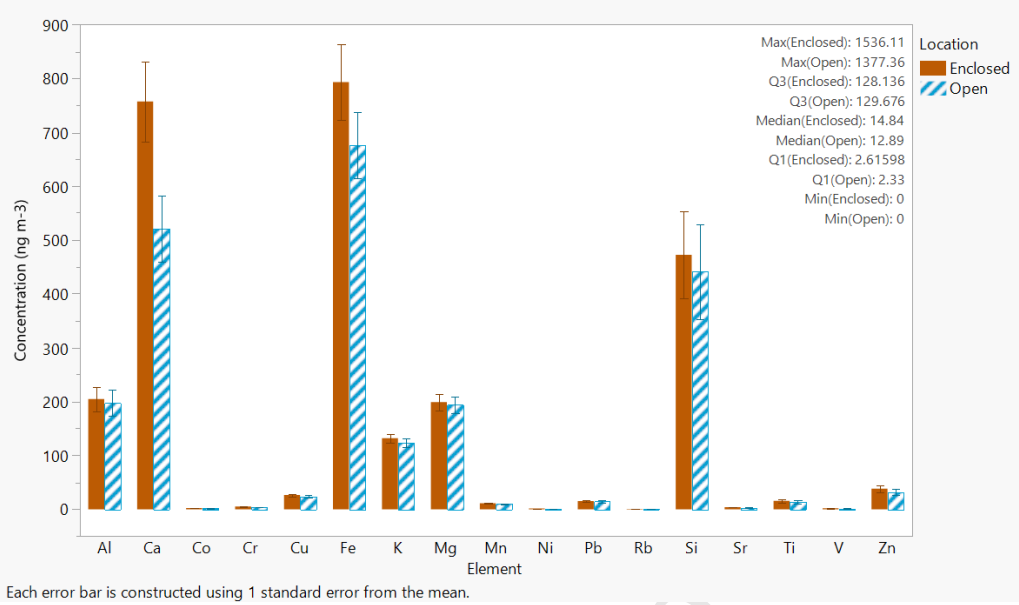

Figure 6: ED-XRF and HR-ICP-MS averaged elemental concentrations (ng m^{-3}), collected at the considered enclosed (brown) and open (blue striped) street canyon sites. The enclosed location (E) exhibited higher median concentrations (ED-XRF and HR-ICP-MS respectively) for Ca (37 and 43%), Fe (6 and 21%), Co (7 and 39%), Ni (11 and 29%), Cu (15 and 27%), Zn (11 and 20%) and Sr (16 and 19%).

When looking at the day-to-day variation of the daily-averaged total element concentrations (ng m^{-3}), similar temporal variation is observed for both analytical techniques (ED-XRF and HR-ICP-MS), confirming the effectiveness of both approaches for analysing PM-loaded filters (Figure 7). Moreover, similar temporal atmospheric concentration variation is observed at both considered monitoring locations (E and O), indicating common contributing pollution sources. As elemental contributions show a significant interaction effect with sampling day ($p<0.0001$), daily PM composition charts are shown in Appendix 8. Largest proportional day-to-day variation is observed for Mn, Pb, Cu, Ca and Ti, followed by Zn, Cr, Fe, Co for the ED-XRF results, while Al, Si, Cr, Ca, Fe and Cu, followed by Mn, Zn, Pb, exhibited largest day-to-day variation in the HR-ICP-MS results.

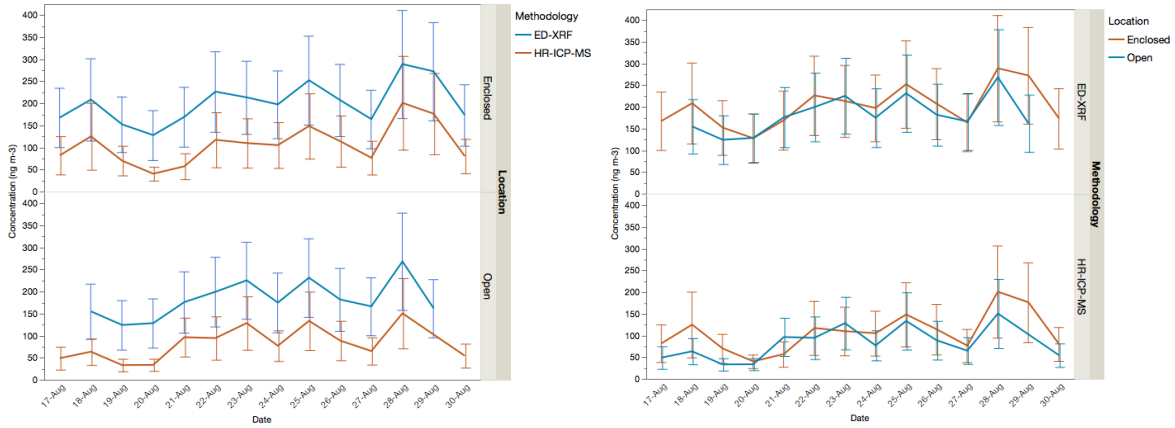

Figure 7: Temporal variation in daily-averaged total element (17) concentration (ng m^{-3}) between the considered methodologies (left; ED-XRF vs HR-ICP-MS) and monitoring sites (right; enclosed vs open). Error bars denote standard errors from the mean.

3.4 Magnetic PM_{10} composition

The daily PM_{10}-loaded filters were analysed for all magnetic properties shown in Table 1. Mass-normalised low-frequency susceptibility (X_{LF} ± standard deviation) of the filters was 12.8 ± 4.27 x 10^{-8} m^3 kg^{-1} and 13.44 ± 4.49 x 10^{-8} m^3 kg^{-1}, for respectively the open and enclosed monitoring location, while the average SIRM amounted to 58186 ± 17261 x 10^{-6} and 61676 ± 15842 x 10^{-6} A m^2 kg^{-1}, respectively.

Table 1: Magnetic results of the daily (August 17-30, 2017) PM_{10}-loaded filters at the open (O) and enclosed (E) monitoring locations.

ID	Date	PM *full* (mg)	PM *half* (mg)	X_{LF} x10^{-8} (m^3/kg)	NRM x10^{-6} (A/m)	$ARM_{200/500}$ x10^{-6} (A/m)	ARMχ x10^{-6} (m^3 kg^{-1})	SIRM x10^{-3} (A m^2 kg^{-1})	IRM_{-300} x10^{-3} (A m^2 kg^{-1})	S-Ratio (-)	HIRM x10^{-3} (A m^2 kg^{-1})	$SIRM/X_{LF}$ x10^{-6} (A m^{-1})	ARM/SIRM x10^{-3} (-)	ARMχ /χLF (-)
O17	17-Aug	0.438	0.219											
O18	18-Aug	0.600	0.300	20.6	26.7	399.8	22.39	95.20	89.57	0.94	2.93	0.46	93.57	108.5
O19	19-Aug	0.711	0.356	11.9	19.8	284.3	13.43	61.63	57.21	0.93	2.30	0.52	86.70	113.0
O20	20-Aug	0.824	0.412	7.60	2.70	250.1	10.20	49.69	46.60	0.94	1.44	0.65	82.22	134.2
O21	21-Aug	0.97	0.485	14.8	94.3	385.7	13.36	70.00	67.10	0.96	1.48	0.47	76.04	90.46
O22	22-Aug	1.158	0.579	16.3	31.6	417.7	12.12	62.34	60.42	0.97	1.02	0.38	77.39	74.25
O23	23-Aug	1.495	0.748	10.5	94.2	487.4	10.95	57.70	54.99	0.95	1.36	0.55	75.69	104.8
O24	24-Aug	0.982	0.491	17.6	632	460	15.74	66.36	61.92	0.93	2.24	0.38	94.54	89.40
O25	25-Aug	1.262	0.631	16.8	40.5	426.6	11.36	73.09	70.37	0.96	1.31	0.43	62.05	67.51
O26	26-Aug	1.573	0.787	9.40	206	385	8.22	37.59	36.01	0.96	0.79	0.40	87.24	87.43
O27	27-Aug	1.257	0.629	9.52	49.5	335.5	8.97	40.47	38.49	0.95	1.02	0.43	88.26	94.15
O28	28-Aug	1.931	0.966	11.2	68.1	555.8	9.67	49.89	47.75	0.96	0.99	0.45	77.55	86.60
O29	29-Aug	2.243	1.122											
O30	30-Aug	1.648	0.824	7.81	63.9	338	6.89	34.29	32.35	0.94	0.98	0.44	80.08	88.18
E17	17-Aug	0.729	0.365	15.5	30.1	303.3	13.98	76.18	72.83	0.96	1.58	0.49	73.37	90.16
E18	18-Aug	0.882	0.441	9.85	37.1	328	12.49	61.21	55.81	0.91	2.63	0.62	81.60	126.9
E19	19-Aug	0.791	0.396	8.34	94.2	302.9	12.87	61.97	56.61	0.92	2.54	0.74	83.17	154.3
E20	20-Aug	0.864	0.432	6.66	22.8	255.1	9.92	49.80	47.29	0.95	1.30	0.75	79.29	149.0
E21	21-Aug	0.769	0.385	18.6	41.7	400.7	17.51	92.91	89.32	0.97	1.59	0.50	75.48	93.87
E22	22-Aug	1.188	0.594	20.6	22.8	522.5	14.78	82.43	78.96	0.96	1.62	0.40	71.71	71.88
E23	23-Aug	1.222	0.611	13.4	41.4	448	12.32	63.38	60.15	0.95	1.53	0.47	77.73	91.78
E24	24-Aug	1.049	0.525	14.6	22.8	398.1	12.75	65.45	60.41	0.92	2.50	0.45	77.74	87.36

E25	25-Aug	1.284	0.642	21.5	38.2	572.2	14.97	75.26	72.33	0.96	1.42	0.35	79.45	69.70
E26	26-Aug	1.708	0.854	11.8	86.1	440.1	8.66	45.50	43.03	0.95	1.09	0.38	76.39	73.48
E27	27-Aug	1.313	0.657	11.5	78.4	334.6	8.56	42.32	40.06	0.94	1.19	0.37	80.48	74.62
E28	28-Aug	2.028	1.014	14.1	22.8	591.6	9.80	50.36	48.40	0.96	0.92	0.36	77.79	69.73
E29	29-Aug	1.823	0.912	13.0	97.6	583.6	10.76	57.92	55.31	0.95	1.32	0.45	74.03	82.97
E30	30-Aug	1.605	0.803	8.77	22.8	379.9	7.95	38.77	36.89	0.95	1.04	0.44	81.38	90.63

3.4.1 Range of magnetic properties

Mass normalised susceptibility and SIRM values from biological accumulation surfaces, e.g. mosses, leaves, bark and trunk wood, crustacea and mammals (-0.9 - 1161 x 10^{-8} m^3 kg^{-1} and 2 – 60000 x 10^{-6} A m^2 kg^{-1}) and human tissues (0.2 - 5.2 x 10^{-8} m^3 kg^{-1} and 0.63 – 63.5 x 10^{-6} A m^2 kg^{-1}) have been recently compiled (Hofman et al., 2017). The magnetic results measured in our study are in line with former reported χ_{LF} and SIRM results obtained from filter-accumulated PM. Shu et al. (2001) reported higher susceptibility (213-2853 x 10^{-8} m^3 kg^{-1}) and SIRM results (20630-548830 x 10^{-6} A m^2 kg^{-1}) from total suspended particles (TSP) at 11 sites across Shanghai, China. . Wang et al. (2017) recently reported on higher susceptibility (131-1900 x 10^{-8} m^3 kg^{-1}) and SIRM (100730-1469570 x 10^{-6} A m^2 kg^{-1}) results from collected $PM_{2.5}$ filters in Nanjing, China, positively associated with Fe, Cd and Pb. Not surprisingly, as average atmospheric $PM_{2.5}$ concentrations in summer and winter in Nanjing amounted to 66.37 and 96.92 µg m^{-3}. Sagnotti et al. (2006) found low-field magnetic susceptibility results in the order of 11-4378 x10^{-8} m^3 kg^{-1} from daily PM_{10} filters over one year in Latium, Italy. Saragnese et al. (2011) report on 20-120 x10^{-8} m^3 kg^{-1} and 30000-210000 x 10^{-6} A m^2 kg^{-1} of daily PM_{10} filters from four monitoring sites in Torino, Italy. Artificial TSP sampling resulted in 297–15847 × 10^{-8} m^3 kg^{-1} in China (Cao et al., 2015) and 14-9533 x 10^{-8} m^3 kg^{-1} and 3100-700000 x 10^{-6} A m^2 kg^{-1} across 38 cities in the state of Tamil Nadu, India (Gargiulo et al., 2016). Our susceptibility (6.66 – 21.5 x 10^{-8} m^3 kg^{-1}) and SIRM (34300-95600 x 10^{-6} A m^2 kg^{-1}) results can therefore be considered realistic, taking into account the smaller particle size range (PM_{10} vs TSP). From One-way ANOVA tests with non-parametric Wilcoxon testing, no significant differences between the considered monitoring locations (E vs O) were observed for the atmospheric PM_{10} concentration (22.35 vs 22.14, $p = 0.84$), SIRM (0.062 vs 0.058, $p = 0.55$) magnetic susceptibility (-6.89 x 10^{-7} vs -7.24 x 10^{-7}, $p = 0.70$) and S-ratio (0.9485 vs 0.9491, $p = 0.96$).

3.4.2 Association with PM mass/concentration

Associations between the PM_{10}-loading of the collected filters and concentration-dependent susceptibility (χ_{LF}; $r = 0.66$, $p < 0.001$, $n = 26$) and *Saturation Isothermal Remanent Magnetisation*

(SIRM; r = 0.63, p < 0.001, n = 26) are observed (Figure 8 and Appendix 10)Moreover, stronger associations were observed at the enclosed street canyon location (Appendix 10).

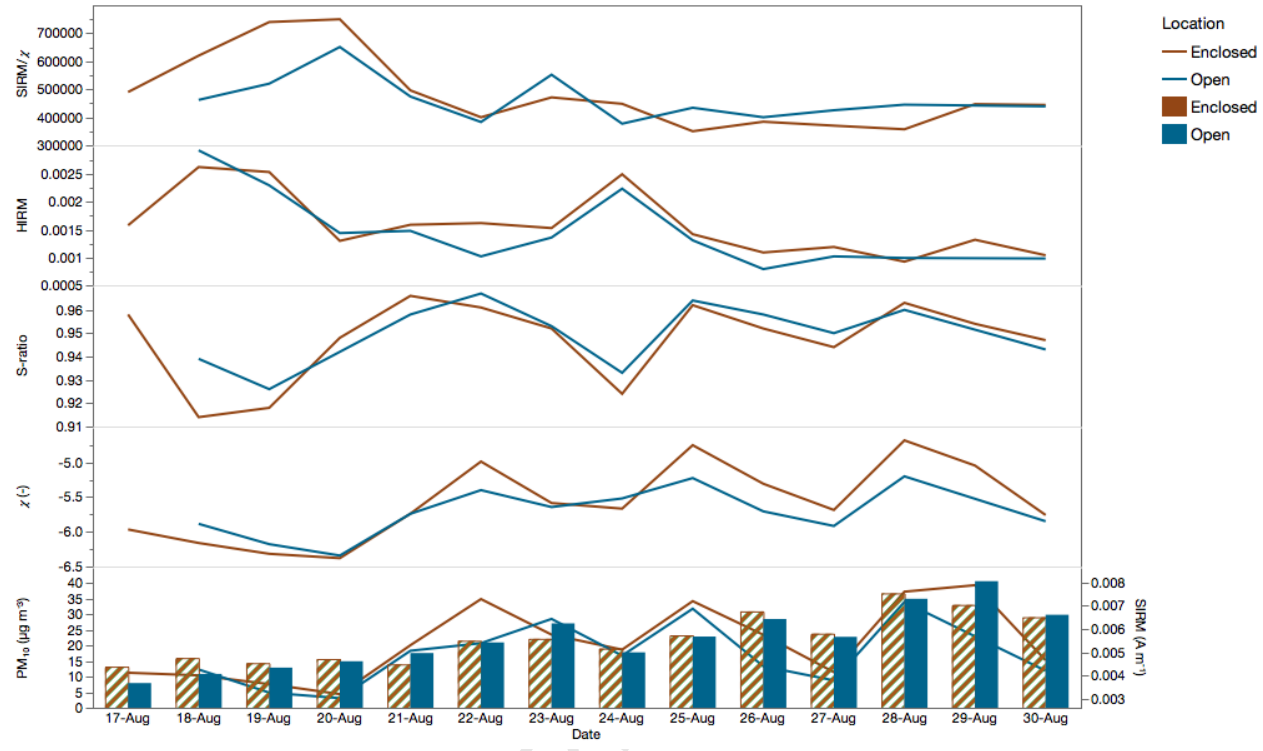

Figure 8: Day-to-day variation in atmospheric PM_{10} concentration (bars) and resulting magnetic properties (lines) at the considered monitoring locations (E; brown and O; blue).

3.4.3 Magnetic mineralogy

From the magnetic bivariate ratios in Table 1 and Figure 8 (S-ratio, HIRM, SIRM/X_{LF}, ARM/SIRM and ARMχ /χ_{LF}), we can conclude that the S-ratio, a measure of the relative contribution of high- ('hard') to low- ('soft') coercivity remanence carriers (Bloemendal et al., 1988; Evans and Heller, 2003), approaches unity (0.92 - 0.97) and is, therefore dominated by the presence of low-coercivity magnetite-type ferromagnetic minerals (Hofman et al., 2017; Wang et al., 2017), e.g. magnetite or maghemite. The HIRM range from 791 to 2930 x 10^{-6} A m^2 kg^{-1}, with a mean value of 1540 x 10^{-6} A m^2 kg^{-1}, corroborates the negligible contribution of antiferromagnetic structures. The high SIRM/X_{LF} (3.5 – 7.5 x 10^5 A m^{-1}) and ARM/SIRM (62.1 – 94.5 x 10^{-3}) ratios are very similar to the results observed by Wang et al. (2017) on $PM_{2.5}$ filters, and point to high contributions of smaller-grained so-called single domain (SD) or pseudo-single domain (PSD) magnetite particles.

3.4.4 Magnetic grain size

Both χ_{ARM} and χ_{LF} increase linearly with increasing magnetite concentration, but as smaller grains are more efficient at acquiring remanence, plotting both parameters on a graph – the so-called King plot – results in higher χ_{ARM} values for smaller grains (King et al., 1982). According to this King plot, the collected PM_{10} samples show similar distributions (magnetic mineralogy) at both locations (enclosed and open), dominated by low concentrated ferrimagnetic carriers with grain sizes below 0.1 µm (Figure 9). Comparing our χ_{ARM} (690 – 1750 x 10^{-8} kg m^{-3}) and χ_{LF} (6.6 - 21.5 x 10^{-8} kg m^{-3}) values against χ_{ARM} (244.4 – 3209 x 10^{-8} kg m^{-3}) and χ_{LF} (130.8 - 1900 x 10^{-8} kg m^{-3}) values from collected atmospheric $PM_{2.5}$ samples during 2013-2014 in Nanjing, China (Wang et al., 2017), reasonable agreement is observed, certainly considering the observed atmospheric concentration differences (8 - 41 vs 66 - 96 µg m^{-3}).

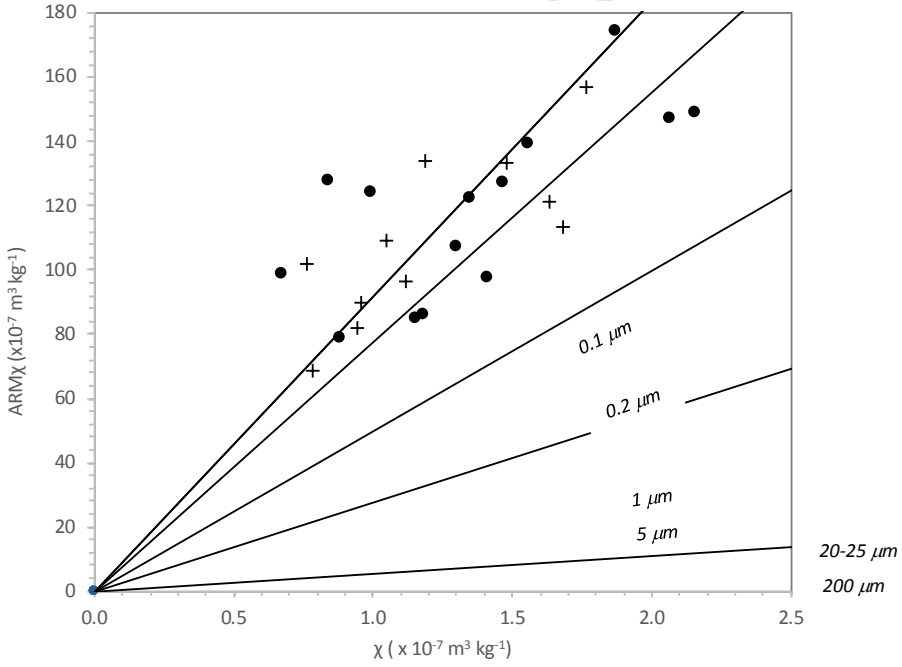

Figure 9: King plot of collected PM_{10} samples at the enclosed (circles) and open (crosses) street canyon locations, with grain size reference lines derived from King et al. (1982).

3.4.5 Trace metal association

The mass concentrations of trace metals reflect variations in contributing particle sources and allow particle toxicity assessment (Wang et al., 2017). HR-ICP-MS trace element mass concentrations (in µg g^{-1}) were used to assess the multivariate linear relationships between the magnetic properties and trace metal content of the filter samples. Concentration-dependent magnetic properties (raw SIRM and susceptibility) showed significant correlations with Fe ($r \sim 0.75$, $p < 0.01$), Cr ($r \sim 0.8$, $p < 0.01$),

Mn (r ~ 0.66 , *p* < *0.05*) and Ti (r ~ 0.6 , p < 0.05), Cu (r ~ 0.64, *p* < *0.05*) and Al (r ~ 0.63, *p* < *0.05*)./The HIRM was significantly linked to K (r = 0.87, *p<0.001*), Mg (r = 0.80, *p* < *0.01*) and Rb (r = 0.61, *p<0.05*), while the S-ratio seems to be associated with Mg (r = -0.63, *p* < *0.05*), Cr (r = 0.62, *p* < *0.05*), Fe (r = 0.61, *p* < *0.05*), Cu (r = 0.68, *p* < *0.05*) and Rb (r = -0.59, *p* < *0.05*).

From the derived correlation clusters (Appendix 11) indicating common source contributions, clusters included Mg, K and Co (1); Mn, Fe, Cu, Cr, Al, Ti, Zn and Pb (2) and V Rb and Ni (3). Cluster 1 might point towards sea spray influences, while cluster 2 suggests a mixture of crustal (Mn, Al, Ti, Ca) and road traffic exhaust (Cu, Fe, Pb) and non-exhaust (Al, Zn, Cu, Cr) sources. V and Ni (cluster 3) are typically linked to heavy oil burning, e.g. shipping or industrial processes(Amato et al., 2011, 2009; Maenhaut et al., 2016; Pandolfi et al., 2016; Vercauteren et al., 2011; Zhang et al., 2012).

3.5 PM_{10}, UFP and BC point measurements

The conducted point measurement campaigns on August, 17, 22, 25, 28 and 30, yielded 1747 10-second measurements for each of the considered pollutants. The temporal atmospheric concentration variation, shown in Figure 10, exhibits day-to-day fluctuations (low: 17/8 and 25/8 vs high: 22/8, 28/8 and 30/8), influenced by meteorology and urban background levels (Hofman et al., 2018, 2016b; Van den Bossche et al., 2015), within-day variation induced by diurnal pollutant variation (e.g. rush hour peaks), and microscale variability, through common local peak events (for all pollutants; e.g. 22/8 at 09:05) or individual local peak events (for single pollutants; e.g. 28/8 at 16:40 for PM_{10}). During the last point measurement campaign (August, 30th), the Dusttrak PM_{10} data was flagged with a low battery warning from 14:59h onwards, clearly leading to compromised data (Figure 10). This data was, therefore, disregarded in the statistical analysis.

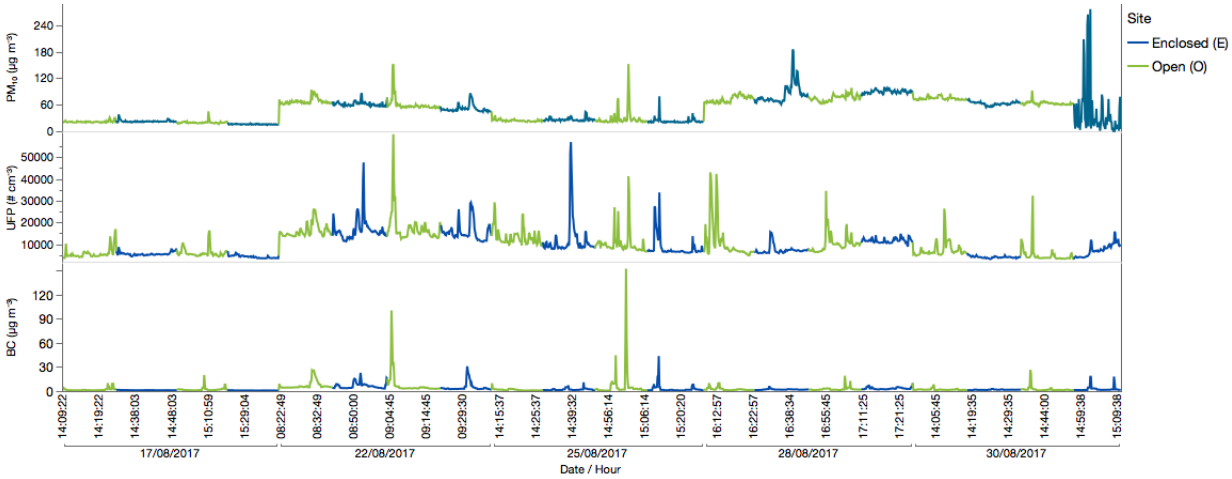

Figure 10: Temporal variation of atmospheric PM_{10} (µg m^{-3}), UFP (# cm^{-3}) and BC (µg m^{-3}) concentrations, collected during the point measurement campaigns at the enclosed (E; blue) and open (O; green) street canyon locations.

When looking at the pollutant microscale variability, several peak events are observed at both the enclosed and open locations. Some common peaks are exhibited for BC, UFP and PM, while other peak events seem to be pollutant-specific. Contradictory to what we expected, One-way ANOVA with non-parametric Wilcoxon testing indicated significantly lower pollutant levels at the enclosed location for BC (2.8 vs 3.7, p=0.02), PM_{10} (48.0 vs 50.9, p<0.001) and UFPs (9206 vs 10230, p<0.001). Site differences seem to be due to the number and intensity of peak events, as similar concentration baselines are observed at both locations. Similar moderate traffic intensities (242 ± 53 vs 264 ± 24) provide no explanation for the observed concentration differences. As we suspected a potential emission source influence of the nearby *Singel* and *R1* ring road, manifested during higher wind speeds, we conducted mobile measurements along a transect through the urban park at the open location towards the *Singel/R1* ring roads under governing south-westerly wind directions (Appendix 12). Nevertheless, no source influence was observed on this monitoring transect.

As a higher pollutant variability seems to be observed on August 22nd and 25th, which are days with prevailing easterly wind directions (Table 2), a potential explanation might be nearby (80 m) façade renovation works of a church. When excluding for days with dominating easterly wind regimes (August 22nd and 25th),location-specific concentration differences (E vs O) are decreased but still significant for BC (1.9 vs 2.2, p = 0.03) and UFPs (6604 vs 7507, p < 0.001), while no significant difference for PM_{10} is observed (52 vs 54, p = 0.24). This observation seems to confirm our

hypothesis as construction works are expected to result in PM peaks, rather than UFP or BC (traffic-related). Moreover, natural PM contributions,originating from the adjacent urban park can not be excluded. The earlier observation of the higher traffic-related metal contributions at the enclosed street canyon location might reflect these non-traffic PM contributions at the open street canyon location.

The presence of a small roundabout near the open location might explain the higher frequency of UFP and BC peaks. Although the absolute traffic intensity is rather similar between both monitoring locations, vehicles will namely accelerate and decelerate more frequently near the roundabout explaning the observed point measurement peaks.

Table 2: Overview of observed traffic intensity (# h^{-1}; sum of low, mid and heavy transport), prevailing wind speed (m s^{-1}) and direction (°) (derived at 30 m height), 15-minute averaged PM_{10} (µg m^{-3}), UFP (# cm^{-3}) and BC (µg m^{-3}) concentrations for each 15-minute interval of the conducted point measurement campaigns at the open (O) and enclosed (E) monitoring locations. Each point measurement campaign consisted of four 15-minute intervals (O1 - E1 - O2 - E2).

		Traffic intensity (# h^{-1})	Wind speed (m s-1)	Wind Direction (°)	PM_{10} (ug m^{-3})	UFP (# cm^{-3})	BC (ug m^{-3})
				Open location (O)			
17-Aug	*O1*	280	5.12	205	21.58	5708	1.92
	O2	252	5.12	205	19.98	6299	2.15
22-Aug	*O1*	280	1.35	89	67.66	16074	7.28
	O2	232	1.35	89	59.83	17470	7.45
25-Aug	*O1*	212	2.49	97	24.13	13106	1.56
	O2	248	2.49	97	28.38	10154	6.90
28-Aug	*O1*	328	2.52	313	72.11	10625	2.43
	O2	332	2.52	313	75.28	10266	2.60
30-Aug	*O1*	212	2.9	240	74.34	7394	1.92
	O2	264	2.9	240	63.28	4902	2.24
	Avg	*264*			*50.66*	*10200*	*3.64*
	stdev	*24*			*23.91*	*4312*	*2.48*
				Enclosed location (E)			
17-Aug	*E1*	220	5.12	205	22.46	5537	1.13
	E2	200	5.12	205	15.68	4138	0.80
22-Aug	*E1*	208	1.35	89	61.78	16743	6.67
	E2	180	1.35	89	50.49	15344	4.84
25-Aug	*E1*	252	2.49	97	26.38	11782	2.09
	E2	260	2.49	97	23.07	8328	2.81
28-Aug	*E1*	244	2.52	313	83.52	7314	2.04
	E2	340	2.52	313	89.84	11686	3.38
30-Aug	*E1*	196	2.9	240	62.63	4016	1.69
	E2	320	2.9	240	40.55	7339	2.60
	Avg	*242*			*47.64*	*9223*	*2.80*
	stdev	*53*			*26.38*	*4487*	*1.78*

4. Conclusions

This study experimentally evaluates the street architecture influence on local pollution levels and composition within a typical urban street canyon (Markgravelei) in Antwerp, Belgium. Our results show that the effect of a street canyon opening, due to a porous urban green patch (Hof van Leysen) did not result in significant ambient PM_{10}, UFP or BC concentration decreases. Although hypothesised otherwise (i), no consistent difference in PM_{10} concentration and magnetic properties was observed between the studied enclosed and open street canyon location. However, on days with favourable (oblique) wind conditions (4 out of 14 days), the natural ventilation hypothesis was supported. Moreover, higher contributions of specific elements at the enclosed street canyon location were identified by both ED-XRF and HR-ICP-MS for Ca (43 vs 37%), Fe (21 vs 6%), Co (39 vs 7%), Ni (29 vs 11%), Cu (27 vs 15%), Zn (20 vs 11%) and Sr (19 vs 16%); elements frequently associated with street dust, derived from road traffic, crustal matter and road wear (hypothesis ii). The variability in wind flow regimes, PM contributions from nearby and non-traffic sources and impact from changing local traffic dynamics (roundabout) seemed to impact these overall outcomes.

Concentration-dependent magnetic properties (SIRM and susceptibility) correlated with the PM_{10} filter loading (and therefore atmospheric PM_{10} concentration), and showed associations with Fe, Cr, Mn and Ti. From the derived magnetic bivariate ratios, magnetic carriers showed to be dominated by low-coercivity magnetite-type ferromagnetic minerals, i.e. small-grained SD or PSD magnetite particles with grain sizes below 0.1 μm; indicating similar magnetic source contributions at both monitoring locations.

Similarly to Karra et al. (2017), our study confirms the complexity of urban flow regimes and resulting pollution levels in real-life urban street canyons. Although the theoretical basis of natural ventilation stands on days with oblique wind flow (4 out of 14), the complexity of variable

wind regimes,the contribution from nearby sourcess and the variability of local traffic dynamics seem to nuance the impact, when compared to theoretical representations of the urban canopy.

Acknowledgements

The authors thank the Flanders Environment Agency (VMM) for their collaboration and air quality and meteorological data. A.C. receives a PhD fellowship (1S21418N) of the Research Foundation Flanders (FWO), while J.H. received a FWO postdoctoral fellowship grant (12I4816N).

Bibliography

Ahmad, K., Khare, M., Chaudhry, K.K., 2005. Wind tunnel simulation studies on dispersion at urban street canyons and intersections—a review. Journal of Wind Engineering and Industrial Aerodynamics 93, 697–717. doi:10.1016/j.jweia.2005.04.002

Alves, C.A., Evtyugina, M., Vicente, A.M.P., Vicente, E.D., Nunes, T.V., Silva, P.M.A., Duarte, M.A.C., Pio, C.A., Amato, F., Querol, X., 2018. Chemical profiling of PM10 from urban road dust. Sci. Total Environ. 634, 41–51. doi:10.1016/j.scitotenv.2018.03.338

Amato, F., Pandolfi, M., Escrig, A., Querol, X., Alastuey, A., Pey, J., Perez, N., Hopke, P.K., 2009. Quantifying road dust resuspension in urban environment by Multilinear Engine: A comparison with PMF2. Atmos. Environ. 43, 2770–2780. doi:10.1016/j.atmosenv.2009.02.039

Amato, F., Pandolfi, M., Moreno, T., Furger, M., Pey, J., Alastuey, A., Bukowiecki, N., Prevot, A.S.H., Baltensperger, U., Querol, X., 2011. Sources and variability of inhalable road dust particles in three European cities. Atmos. Environ. 45, 6777–6787. doi:10.1016/j.atmosenv.2011.06.003

Bloemendal, J., Lamb, B., King, J., 1988. Paleoenvironmental implications of rock-magnetic properties of Late Quaternary sediment cores from the eastern equatorial Atlantic. Paleoceanography 3, 61–87. doi:10.1029/PA003i001p00061

Buccolieri, R., Gromke, C., Di Sabatino, S., Ruck, B., 2009. Aerodynamic effects of trees on pollutant concentration in street canyons. Sci. Total Environ. 407, 5247–5256. doi:10.1016/j.scitotenv.2009.06.016

Cao, L., Appel, E., Hu, S., Ma, M., 2015. An economic passive sampling method to detect particulate pollutants using magnetic measurements. Environ. Pollut. 205, 97–102. doi:10.1016/j.envpol.2015.05.019

Custer, T.W., Custer, C.M., Hines, R.K., Sparks, D.W., 2000. Trace elements, organochlorines, polycyclic aromatic hydrocarbons, dioxins, and furans in lesser scaup wintering on the Indiana Harbor Canal. Environ. Pollut. 110, 469–482.

Dedik, A.N., Hoffmann, P., Ensling, J., 1992. Chemical characterization of iron in atmospheric aerosols. Atmospheric Environment. Part A. General Topics 26, 2545–2548. doi:10.1016/0960-1686(92)90106-U

Evans, M.E., Heller, F., 2003. Environmental Magnetism: Principles and Applications of Enviromagnetics, 1st ed. Elsevier Science, California, USA.

Galvão, E.S., Santos, J.M., Lima, A.T., Reis, N.C., Orlando, M.T.D., Stuetz, R.M., 2018. Trends in analytical techniques applied to particulate matter characterization: A critical review of fundaments and applications. Chemosphere 199, 546–568. doi:10.1016/j.chemosphere.2018.02.034

Gargiulo, J.D., Kumar, R.S., Chaparro, Marcos A.E., Chaparro, Mauro A.E., Natal, M., Rajkumar, P., 2016. Magnetic properties of air suspended particles in thirty eight cities from south India. Atmos. Pollut. Res. 7, 626–637. doi:10.1016/j.apr.2016.02.008

Goryainova, Z., Vuković, G., Urošević, M.A., Vergel, K., Ostrovnaya, T., Frontasyeva, M., Zechmeister, H., 2016. Assessment of vertical element distribution in street canyons using the moss Sphagnum girgensohnii: A case study in Belgrade and Moscow cities. Atmos. Pollut. Res. 7, 690–697. doi:10.1016/j.apr.2016.02.013

Gromke, C., Ruck, B., 2007. Influence of trees on the dispersion of pollutants in an urban street canyon—Experimental investigation of the flow and concentration field. Atmos. Environ. 41, 3287–3302. doi:10.1016/j.atmosenv.2006.12.043

Gromke, C., Ruck, B., 2012. Pollutant Concentrations in Street Canyons of Different Aspect Ratio with Avenues of Trees for Various Wind Directions. Boundary Layer Meteorol. 144, 41–64. doi:10.1007/s10546-012-9703-z

Hama, S.M.L., Cordell, R.L., Staelens, J., Mooibroek, D., Monks, P.S., 2018. Chemical composition and source identification of PM 10' ' in five North Western European cities. Atmos. Res. doi:10.1016/j.atmosres.2018.07.014

Hansard, R., Maher, B.A., Kinnersley, R., 2011. Biomagnetic monitoring of industry-derived particulate pollution. Environ. Pollut. 159, 1673–1681. doi:10.1016/j.envpol.2011.02.039

Hansard, R., Maher, B.A., Kinnersley, R.P., 2012. Rapid magnetic biomonitoring and differentiation of atmospheric particulate pollutants at the roadside and around two major industrial sites in the U.K. Environ. Sci. Technol. 46, 4403–4410. doi:10.1021/es203275r

Harrison, R.M., Jones, A.M., Gietl, J., Yin, J., Green, D.C., 2012. Estimation of the contributions of brake dust, tire wear, and resuspension to nonexhaust traffic particles derived from atmospheric measurements. Environ. Sci. Technol. 46, 6523–6529. doi:10.1021/es300894r

Hofman, J., Bartholomeus, H., Janssen, S., Calders, K., Wuyts, K., Van Wittenberghe, S., Samson, R., 2016a. Influence of tree crown characteristics on the local PM10 distribution inside an urban street canyon in Antwerp (Belgium): A model and experimental approach. Urban Forestry & Urban Greening 20, 265–276. doi:10.1016/j.ufug.2016.09.013

Hofman, J., Maher, B.A., Muxworthy, A.R., Wuyts, K., Castanheiro, A., Samson, R., 2017. Biomagnetic Monitoring of Atmospheric Pollution: A Review of Magnetic Signatures from Biological Sensors. Environ. Sci. Technol. 51, 6648–6664. doi:10.1021/acs.est.7b00832

Hofman, J., Samson, R., Joosen, S., Blust, R., Lenaerts, S., 2018. Cyclist exposure to black carbon, ultrafine particles and heavy metals: An experimental study along two commuting routes near Antwerp, Belgium. Environ. Res. 164, 530–538. doi:10.1016/j.envres.2018.03.004

Hofman, J., Staelens, J., Cordell, R., Stroobants, C., Zikova, N., Hama, S.M.L., Wyche, K.P., Kos, G.P.A., Van Der Zee, S., Smallbone, K.L., Weijers, E.P., Monks, P.S., Roekens, E., 2016b. Ultrafine particles in four European urban environments: Results from a new continuous long-term monitoring network. Atmospheric Environment 136, 68–81.

Hofman, J., Stokkaer, I., Snauwaert, L., Samson, R., 2013. Spatial distribution assessment of particulate matter in an urban street canyon using biomagnetic leaf monitoring of tree crown deposited particles. Environ. Pollut. 183, 123–132. doi:10.1016/j.envpol.2012.09.015

Janhäll, S., 2015. Review on urban vegetation and particle air pollution – Deposition and dispersion. Atmos. Environ. 105, 130–137. doi:10.1016/j.atmosenv.2015.01.052

Jeanjean, A., Buccolieri, R., Eddy, J., Monks, P., Leigh, R., 2017. Air quality affected by trees in real street canyons: the case of Marylebone neighbourhood in central London. Urban Forestry & Urban Greening 22, 41–53. doi:10.1016/j.ufug.2017.01.009

Karra, S., Malki-Epshtein, L., Neophytou, M., 2011. The Dispersion of Traffic Related Pollutants Across a Non-Homogeneous Street Canyon. Procedia Environmental Sciences 4, 25–34. doi:10.1016/j.proenv.2011.03.004

Karra, S., Malki-Epshtein, L., Neophytou, M.K.-A., 2017. Air flow and pollution in a real, heterogeneous urban street canyon: A field and laboratory study. Atmos. Environ. 165, 370–384. doi:10.1016/j.atmosenv.2017.06.035

Kelly, F.J., Fussell, J.C., 2012. Size, source and chemical composition as determinants of toxicity attributable to ambient particulate matter. Atmos. Environ. 60, 504–526. doi:10.1016/j.atmosenv.2012.06.039

Keuken, M.P., Moerman, M., Voogt, M., Blom, M., Weijers, E.P., Röckmann, T., Dusek, U., 2013. Source contributions to PM2.5 and PM10 at an urban background and a street location. Atmos. Environ. 71, 26–35. doi:10.1016/j.atmosenv.2013.01.032

Kim, W., Doh, S.-J., Yu, Y., 2009. Anthropogenic contribution of magnetic particulates in urban roadside dust. Atmos. Environ. 43, 3137–3144. doi:10.1016/j.atmosenv.2009.02.056

King, J., Banerjee, S.K., Marvin, J., Özdemir, Ö., 1982. A comparison of different magnetic methods for determining the relative grain size of magnetite in natural materials: Some results from lake sediments. Earth Planet. Sci. Lett. 59, 404–419. doi:10.1016/0012-821X(82)90142-X

Kumar, P., Ketzel, M., Vardoulakis, S., Pirjola, L., Britter, R., 2011. Dynamics and dispersion modelling of nanoparticles from road traffic in the urban atmospheric environment—A review. J. Aerosol Sci. 42, 580–603. doi:10.1016/j.jaerosci.2011.06.001

Lu, S., Yu, X., Chen, Y., 2016. Magnetic properties, microstructure and mineralogical phases of technogenic magnetic particles (TMPs) in urban soils: Their source identification and environmental implications. Sci. Total Environ. 543, 239–247. doi:10.1016/j.scitotenv.2015.11.046

Ma, M., Hu, S., Cao, L., Appel, E., Wang, L., 2015. Atmospheric pollution history at Linfen (China) uncovered by magnetic and chemical parameters of sediments from a water reservoir. Environ. Pollut. 204, 161–172. doi:10.1016/j.envpol.2015.04.028

Maenhaut, W., Vermeylen, R., Claeys, M., Vercauteren, J., Roekens, E., 2016. Sources of the PM10 aerosol in Flanders, Belgium, and re-assessment of the contribution from wood burning. Sci. Total Environ. 562, 550–560. doi:10.1016/j.scitotenv.2016.04.074

Magiera, T., Jabłońska, M., Strzyszcz, Z., Rachwal, M., 2011. Morphological and mineralogical forms of technogenic magnetic particles in industrial dusts. Atmos. Environ. 45, 4281–4290. doi:10.1016/j.atmosenv.2011.04.076

Maher, B.A., Ahmed, I.A.M., Karloukovski, V., MacLaren, D.A., Foulds, P.G., Allsop, D., Mann, D.M.A., Torres-Jardón, R., Calderon-Garciduenas, L., 2016. Magnetite pollution nanoparticles in the human brain. Proc. Natl. Acad. Sci. USA 113, 10797–10801. doi:10.1073/pnas.1605941113

Maher, B.A., Thompson, R., Hounslow, M.W., 1999. Introduction, in: Maher, Barbara A., Thompson, Roy (Eds.), Quaternary Climates, Environments and Magnetism. Cambridge University Press, Cambridge, pp. 1–48. doi:10.1017/CBO9780511535635.002

Mantovani, L., Tribaudino, M., Solzi, M., Barraco, V., De Munari, E., Pironi, C., 2018. Magnetic and SEM-EDS analyses of Tilia cordata leaves and PM10 filters as a complementary source of information on polluted air: Results from the city of Parma (Northern Italy). Environ. Pollut. 239, 777–787. doi:10.1016/j.envpol.2018.04.055

Matzka, J., Maher, B.A., 1999. Magnetic biomonitoring of roadside tree leaves: identification of spatial and temporal variations in vehicle-derived particulates. Atmos. Environ. 33, 4565–4569. doi:10.1016/S1352-2310(99)00229-0

Morakinyo, T.E., Lam, Y.F., 2016. Study of traffic-related pollutant removal from street canyon with trees: dispersion and deposition perspective. Environ. Sci. Pollut. Res. 23, 21652–21668. doi:10.1007/s11356-016-7322-9

Moretti, S., Smets, W., Mubiana, K.V., Oerlemans, E., Hofman, J., Vandenheuvel, D., Samson, R., Blust, R., Lebeer, S., 2018. Inflammatory response in vitro by endotoxins in urban air samples and association with transition metals. Particle and Fibre Toxicology (PFT).

Muxworthy, A.R., Matzka, J., Davila, A.F., Petersen, N., 2003. Magnetic signature of daily sampled urban atmospheric particles. Atmos. Environ. 37, 4163–4169. doi:10.1016/S1352-2310(03)00500-4

Ng, W.-Y., Chau, C.-K., 2014. A modeling investigation of the impact of street and building configurations on personal air pollutant exposure in isolated deep urban canyons. Sci. Total Environ. 468-469, 429–448. doi:10.1016/j.scitotenv.2013.08.077

Nicholson, S.E., 1975. A pollution model for street-level air. Atmos. Environ. 9, 19–31. doi:10.1016/0004-6981(75)90051-7

Nikolova, I., Janssen, S., Vos, P., Vrancken, K., Mishra, V., Berghmans, P., 2011. Dispersion modelling of traffic induced ultrafine particles in a street canyon in Antwerp, Belgium and comparison with observations. Sci. Total Environ. 412-413, 336–343. doi:10.1016/j.scitotenv.2011.09.081

Oldfield, F., Scoullos, M., 1984. Particulate pollution monitoring in the Elefsis Gulf: The role of mineral magnetic studies. Mar. Pollut. Bull. 15, 229–231. doi:10.1016/0025-326X(84)90294-7

Pandolfi, M., Alastuey, A., Pérez, N., Reche, C., Castro, I., Shatalov, V., Querol, X., 2016. Trends analysis of PM source contributions and chemical tracers in NE Spain during 2004–2014: a multi-exponential approach. Atmos. Chem. Phys. 16, 11787–11805. doi:10.5194/acp-16-11787-2016

Pirjola, L., Lähde, T., Niemi, J.V., Kousa, A., Rönkkö, T., Karjalainen, P., Keskinen, J., Frey, A., Hillamo, R., 2012. Spatial and temporal characterization of traffic emissions in urban microenvironments with a mobile laboratory. Atmos. Environ. 63, 156–167. doi:10.1016/j.atmosenv.2012.09.022

Pugh, T.A.M., Mackenzie, A.R., Whyatt, J.D., Hewitt, C.N., 2012. Effectiveness of green infrastructure for improvement of air quality in urban street canyons. Environ. Sci. Technol. 46, 7692–7699. doi:10.1021/es300826w

Rai, P.K., 2013. Environmental magnetic studies of particulates with special reference to biomagnetic monitoring using roadside plant leaves. Atmos. Environ. 72, 113–129. doi:10.1016/j.atmosenv.2013.02.041

Sagnotti, L., Macrì, P., Egli, R., Mondino, M., 2006. Magnetic properties of atmospheric particulate matter from automatic air sampler stations in Latium (Italy): Toward a definition of magnetic fingerprints for natural and anthropogenic PM10 sources. J. Geophys. Res. 111. doi:10.1029/2006JB004508

Sanderson, P., Su, S.S., Chang, I.T.H., Delgado Saborit, J.M., Kepaptsoglou, D.M., Weber, R.J.M., Harrison, R.M., 2016. Characterisation of iron-rich atmospheric submicrometre particles in the roadside environment. Atmos. Environ. 140, 167–175. doi:10.1016/j.atmosenv.2016.05.040

Sant'Ovaia, H., Marques, G., Santos, A., Gomes, C., Rocha, A., 2015. Magnetic susceptibility and isothermal remanent magnetization in human tissues: a study case. Biometals 28, 951–958. doi:10.1007/s10534-015-9879-z

Saragnese, F., Lanci, L., Lanza, R., 2011. Nanometric-sized atmospheric particulate studied by magnetic analyses. Atmos. Environ. 45, 450–459. doi:10.1016/j.atmosenv.2010.09.057

Schatzmann, M., Leitl, B., Liedtke, J., 2000. Dispersion in Urban Environments; Comparison of Field Measurements with Wind Tunnel Results. Environ. Monit. Assess.

Shu, J., Dearing, J.A., Morse, A.P., Yu, L., Yuan, N., 2001. Determining the sources of atmospheric particles in Shanghai, China, from magnetic and geochemical properties. Atmos. Environ. 35, 2615–2625. doi:10.1016/S1352-2310(00)00454-4

Spassov, S., Egli, R., Heller, F., Nourgaliev, D.K., Hannam, J., 2004. Magnetic quantification of urban pollution sources in atmospheric particulate matter. Geophys. J. Int. 159, 555–564. doi:10.1111/j.1365-246X.2004.02438.x

Thompson, R., Oldfield, F., 1986. Magnetic minerals and environmental systems, in: Environmental Magnetism. Springer Netherlands, Dordrecht, pp. 65–71. doi:10.1007/978-94-011-8036-8_7

Van den Bossche, J., Peters, J., Verwaeren, J., Botteldooren, D., Theunis, J., De Baets, B., 2015. Mobile monitoring for mapping spatial variation in urban air quality: Development and validation of a methodology based on an extensive dataset. Atmos. Environ. 105, 148–161. doi:10.1016/j.atmosenv.2015.01.017

Vardoulakis, S., Fisher, B.E.., Pericleous, K., Gonzalez-Flesca, N., 2003. Modelling air quality in street canyons: a review. Atmos. Environ. 37, 155–182. doi:10.1016/S1352-2310(02)00857-9

Vercauteren, J., Matheeussen, C., Wauters, E., Roekens, E., van Grieken, R., Krata, A., Makarovska, Y., Maenhaut, W., Chi, X., Geypens, B., 2011. Chemkar PM10: An extensive look at the local differences in chemical composition of PM10 in Flanders, Belgium. Atmos. Environ. 45, 108–116. doi:10.1016/j.atmosenv.2010.09.040

Vos, P.E.J., Maiheu, B., Vankerkom, J., Janssen, S., 2013. Improving local air quality in cities: to tree or not to tree? Environ. Pollut. 183, 113–122. doi:10.1016/j.envpol.2012.10.021

Vranckx, S., Vos, P., Maiheu, B., Janssen, S., 2015. Impact of trees on pollutant dispersion in street canyons: A numerical study of the annual average effects in Antwerp, Belgium. Sci. Total Environ. 532, 474–483. doi:10.1016/j.scitotenv.2015.06.032

Wang, G., Oldfield, F., Xia, D., Chen, F., Liu, X., Zhang, W., 2012. Magnetic properties and correlation with heavy metals in urban street dust: A case study from the city of Lanzhou, China. Atmos. Environ. 46, 289–298. doi:10.1016/j.atmosenv.2011.09.059

Wang, J., Li, S., Li, H., Qian, X., Li, X., Liu, X., Lu, H., Wang, C., Sun, Y., 2017. Trace metals and magnetic particles in PM2.5: Magnetic identification and its implications. Sci. Rep. 7, 9865. doi:10.1038/s41598-017-08628-0

Wania, A., Bruse, M., Blond, N., Weber, C., 2012. Analysing the influence of different street vegetation on traffic-induced particle dispersion using microscale simulations. J. Environ. Manage. 94, 91–101. doi:10.1016/j.jenvman.2011.06.036

Weber, S., Hoffmann, P., Ensling, J., Dedik, A.N., Weinbruch, S., Miehe, G., Gütlich, P., Ortner, H.M., 2000. Characterization of iron compounds from urban and rural aerosol sources. J. Aerosol Sci. 31, 987–997. doi:10.1016/S0021-8502(99)00564-9

Yang, T., Liu, Q., Li, H., Zeng, Q., Chan, L., 2010. Anthropogenic magnetic particles and heavy metals in the road dust: Magnetic identification and its implications. Atmos. Environ. 44, 1175–1185. doi:10.1016/j.atmosenv.2009.12.028

Zhang, C., Qiao, Q., Appel, E., Huang, B., 2012. Discriminating sources of anthropogenic heavy metals in urban street dusts using magnetic and chemical methods. J. Geochem. Explor. 119-120, 60–75. doi:10.1016/j.gexplo.2012.06.014

Declaration of interests

☒ The authors declare that they have no known competing financial interests or personal relationships that could have appeared to influence the work reported in this paper.

☐The authors declare the following financial interests/personal relationships which may be considered as potential competing interests:

Highlights:

- Real-life experimental study on natural ventilation in a typical urban street canyon
- Atmospheric PM_{10} concentration and analytical magneto-chemical composition
- Natural ventilation was suggested under oblique wind regimes, but net effect was negligible
- Higher contributions of Ca, Fe, Co, Ni, Cu, Zn and Sr at the enclosed location
- Holistic approach contributes to a better understanding on urban pollution ventilation


Enclosed
© 2018 Google
Google Earth
R802
R801
E
O
Image Landsat / Copernicus
R817
Google Earth
Enclosed (E)
Open (O)
© 2018 Google
© 2018 Google
Open

Figure 1

Figure 2

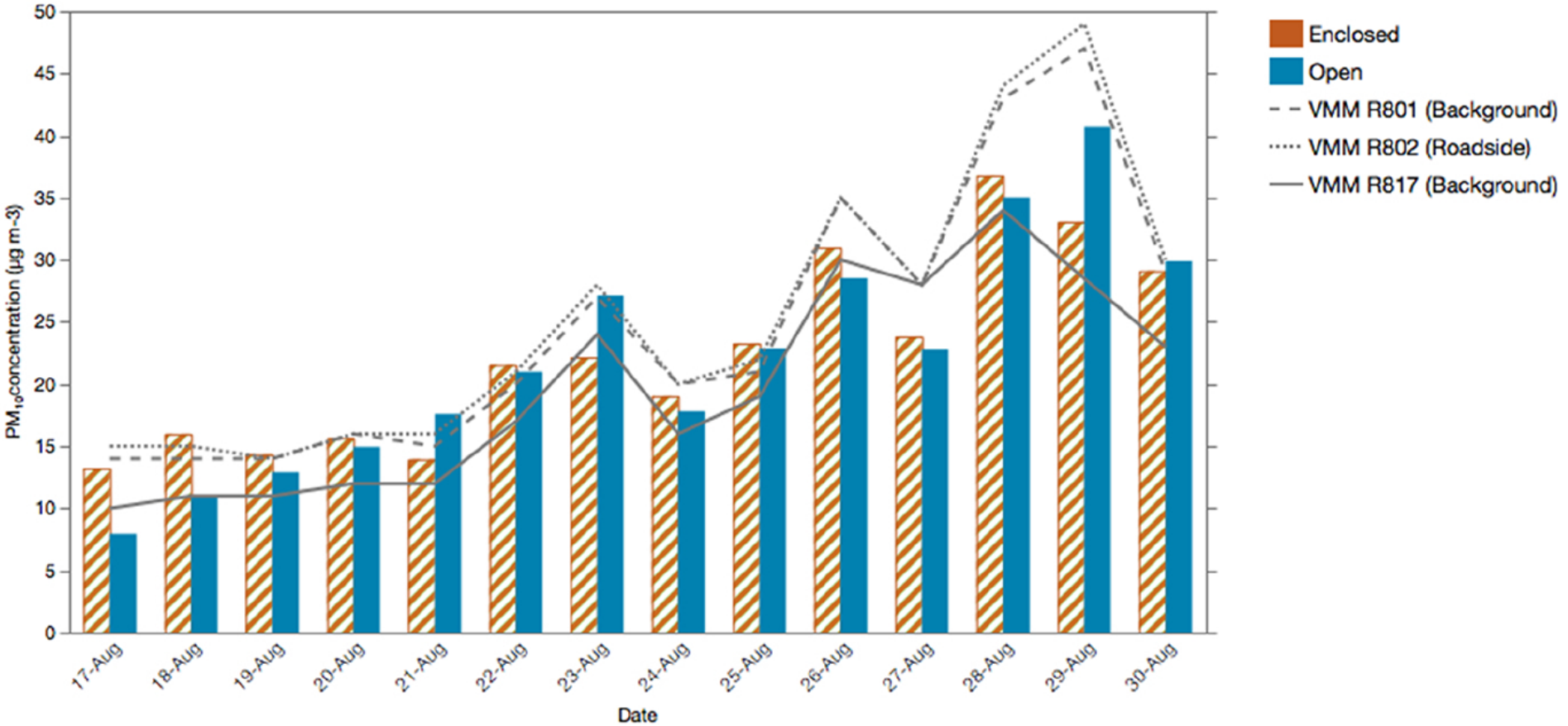
Enclosed
Open
VMM R801 (Background)
VMM R802 (Roadside)
VMM R817 (Background)
PM10 concentration (µg m-3)
0
5
10
15
20
25
30
35
40
45
50
17-Aug
18-Aug
19-Aug
20-Aug
21-Aug
22-Aug
23-Aug
24-Aug
25-Aug
26-Aug
27-Aug
28-Aug
29-Aug
30-Aug
Date

Figure 3

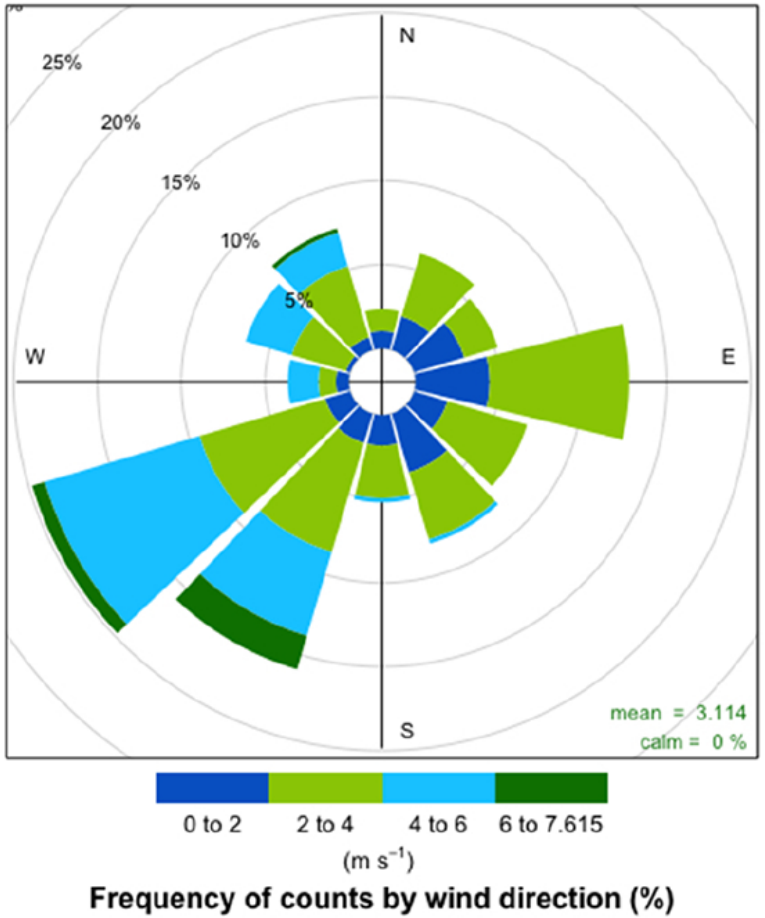
N
E
S
W
25%
20%
15%
10%
5%
mean = 3.114
calm = 0 %
0 to 2
2 to 4
4 to 6
6 to 7.615
(m s⁻¹)
Frequency of counts by wind direction (%)

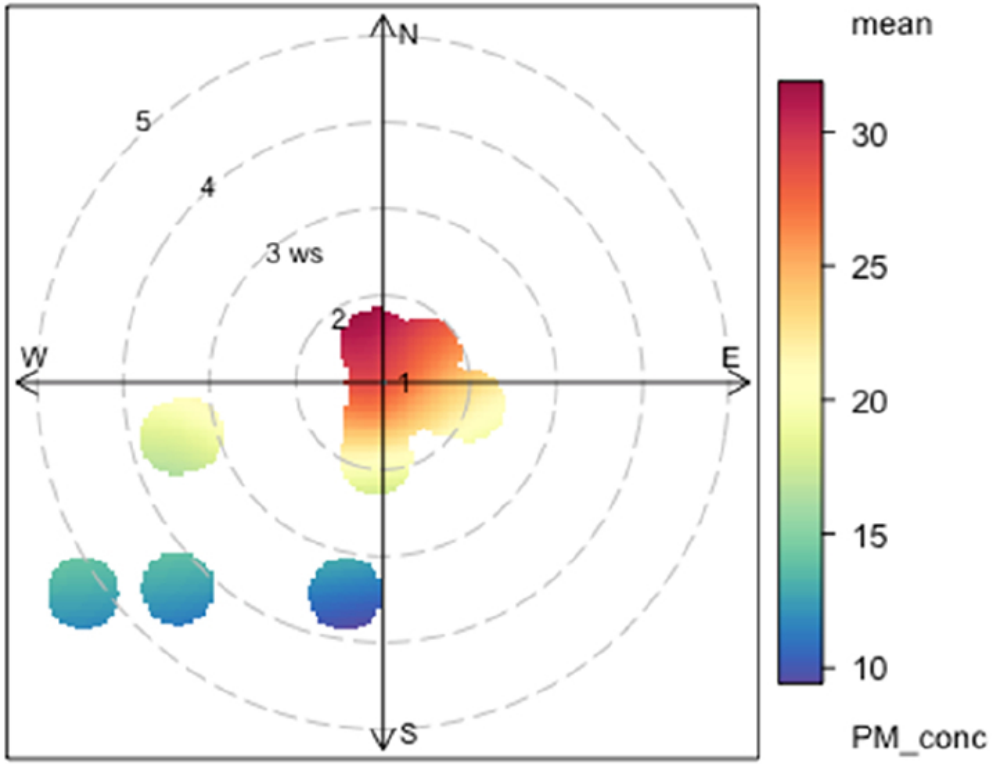
N
E
S
W
5
4
3 ws
2
1
mean
30
25
20
15
10
PM_conc

Figure 4

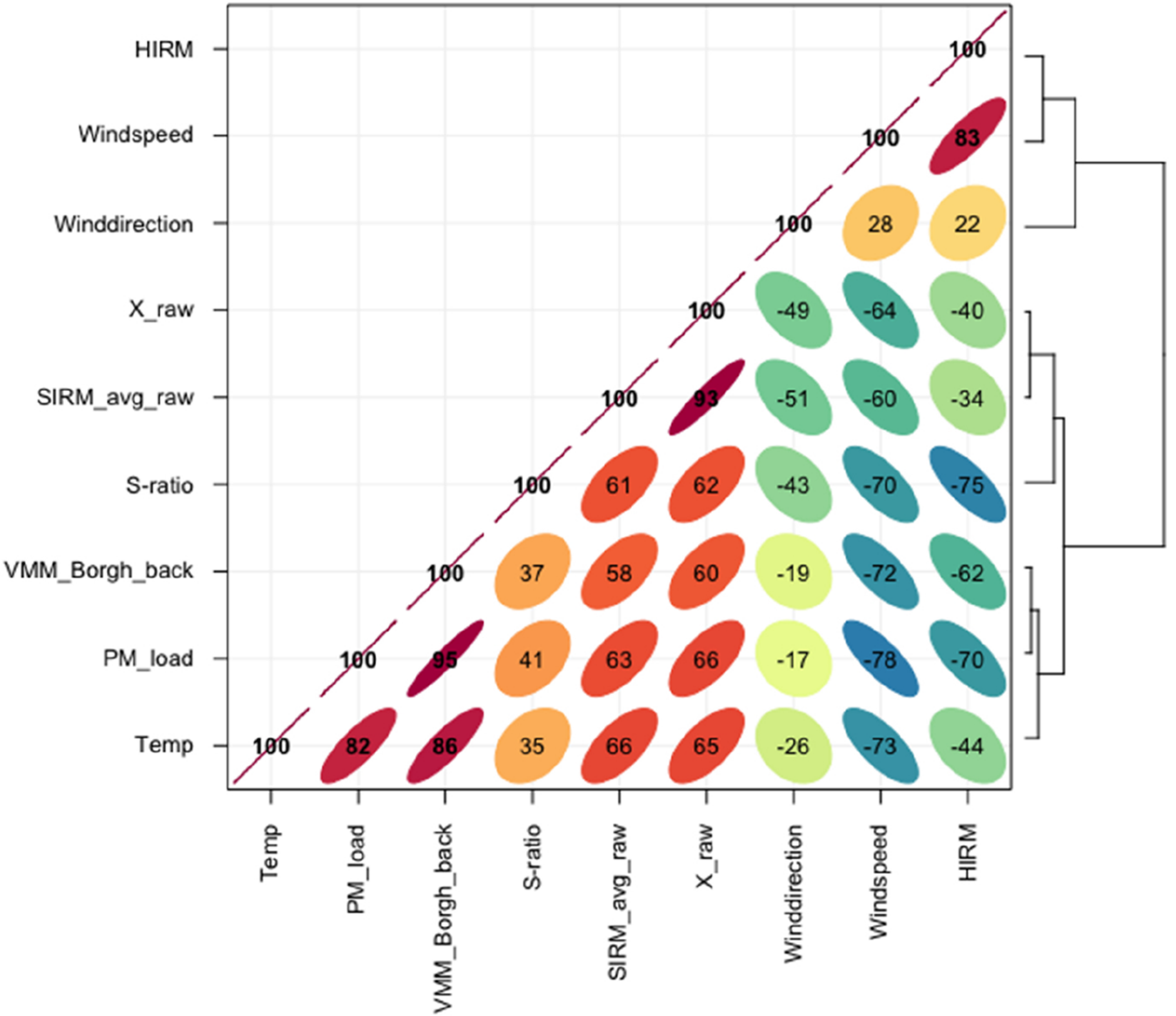
HIRM
Windspeed
Winddirection
X_raw
SIRM_avg_raw
S-ratio
VMM_Borgh_back
PM_load
Temp
100
100 83
100 28 22
100 -49 -64 -40
100 93 -51 -60 -34
100 61 62 -43 -70 -75
100 37 58 60 -19 -72 -62
100 95 41 63 66 -17 -78 -70
100 82 86 35 66 65 -26 -73 -44
Temp
PM_load
VMM_Borgh_back
S-ratio
SIRM_avg_raw
X_raw
Winddirection
Windspeed
HIRM

Figure 5

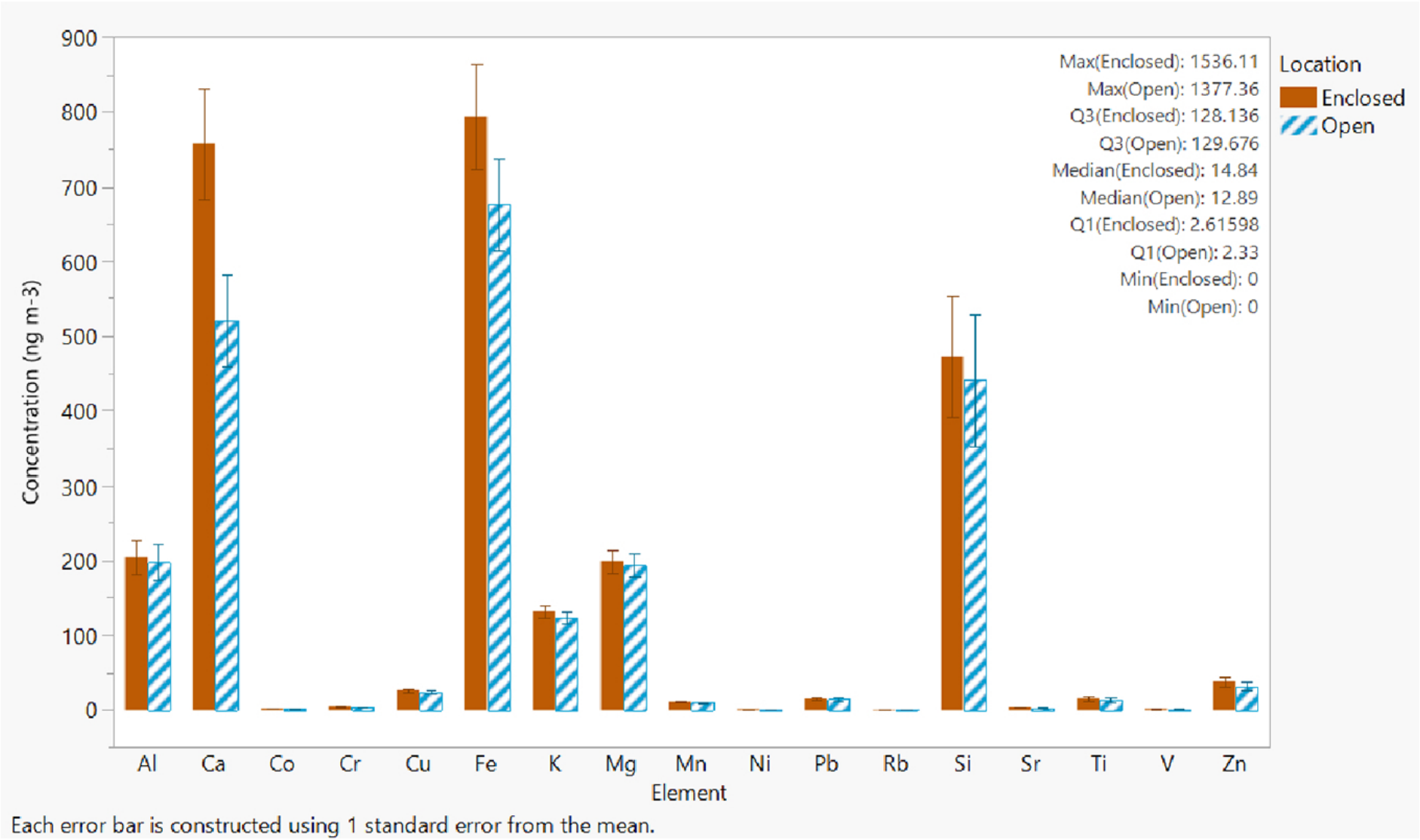
Max(Enclosed): 1536.11
Max(Open): 1377.36
Q3(Enclosed): 128.136
Q3(Open): 129.676
Median(Enclosed): 14.84
Median(Open): 12.89
Q1(Enclosed): 2.61598
Q1(Open): 2.33
Min(Enclosed): 0
Min(Open): 0
Location
Enclosed
Open
Concentration (ng m-3)
900
800
700
600
500
400
300
200
100
0
Al
Ca
Co
Cr
Cu
Fe
K
Mg
Mn
Ni
Pb
Rb
Si
Sr
Ti
V
Zn
Element
Each error bar is constructed using 1 standard error from the mean.

Figure 6

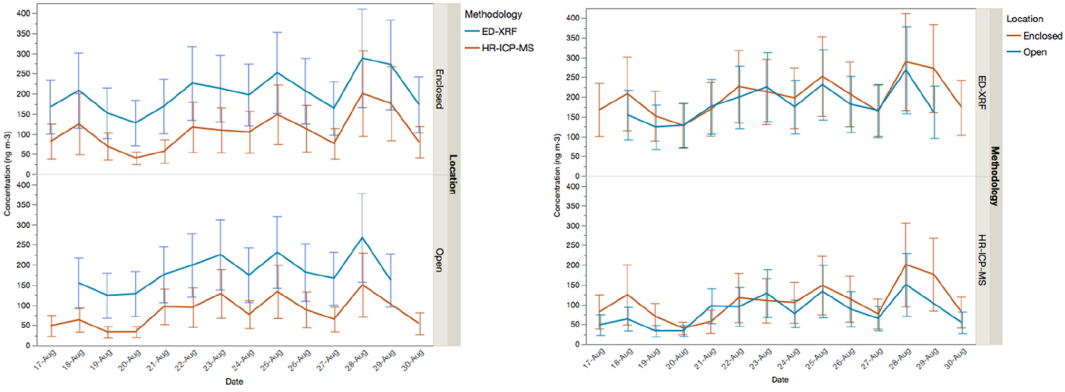
Methodology
ED-XRF
HR-ICP-MS
Location
Enclosed
Open
Concentration (ng m-3)
Date
17-Aug
18-Aug
19-Aug
20-Aug
21-Aug
22-Aug
23-Aug
24-Aug
25-Aug
26-Aug
27-Aug
28-Aug
29-Aug
30-Aug

Figure 7

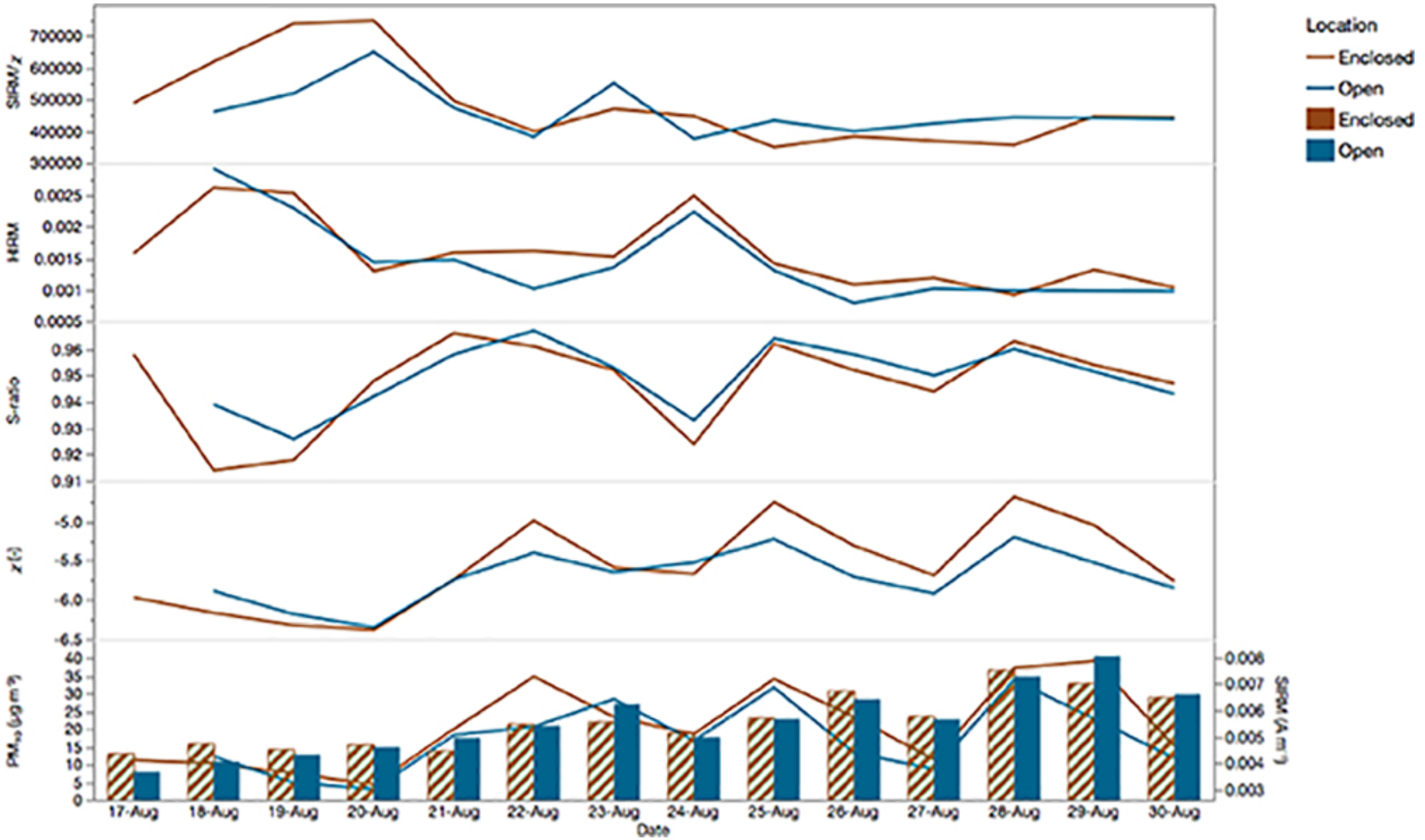
Location
Enclosed
Open
Enclosed
Open
SIRM/χ
IRM
S-ratio
χ (-)
PM10 (µg m-3)
SIRM (A m-1)
Date
17-Aug
18-Aug
19-Aug
20-Aug
21-Aug
22-Aug
23-Aug
24-Aug
25-Aug
26-Aug
27-Aug
28-Aug
29-Aug
30-Aug

Figure 8

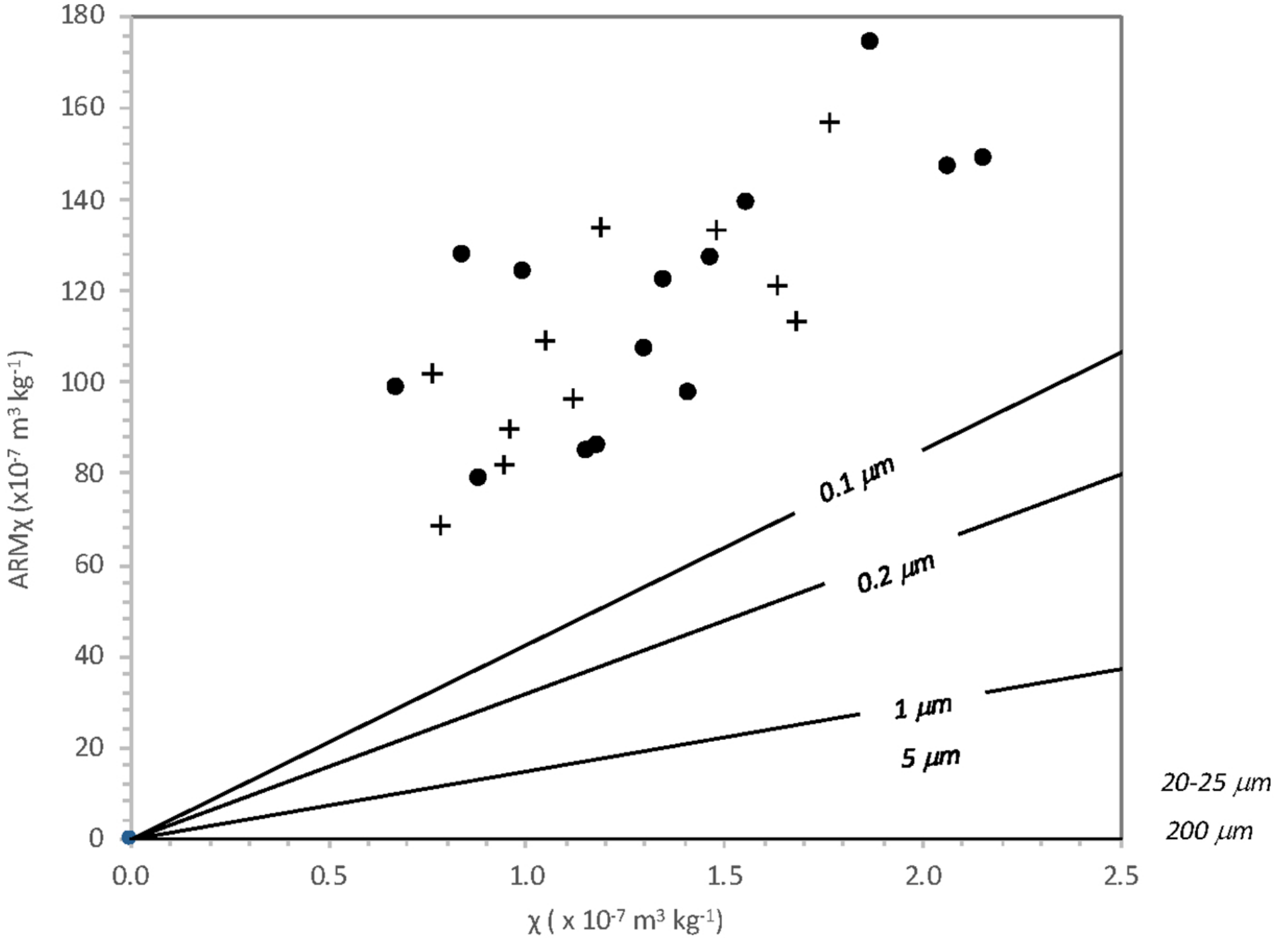
180
160
140
120
100
80
60
40
20
0
ARMχ (x10-7 m3 kg-1)
0.0
0.5
1.0
1.5
2.0
2.5
χ (x 10-7 m3 kg-1)
0.1 μm
0.2 μm
1 μm
5 μm
20-25 μm
200 μm

Figure 9

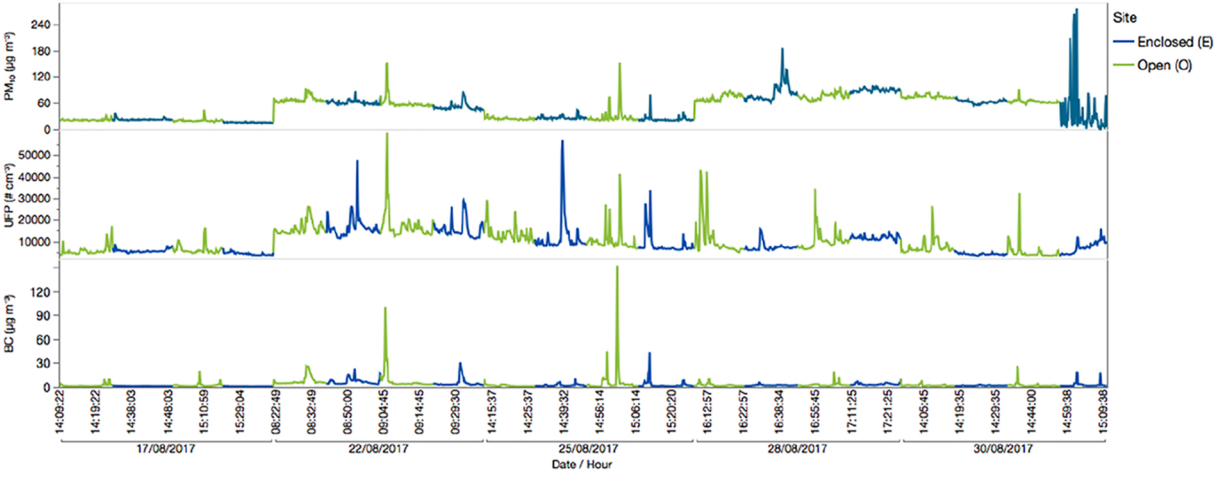
Site
Enclosed (E)
Open (O)
PM10 (µg m-3)
240
180
120
60
0
UFP (# cm-3)
50000
40000
30000
20000
10000
BC (µg m-3)
120
90
60
30
0
14:09:22
14:19:22
14:38:03
14:48:03
15:10:59
15:29:04
06:22:49
06:32:49
06:50:00
09:04:45
09:14:45
09:29:30
14:15:37
14:25:37
14:39:32
14:56:14
15:06:14
15:20:20
16:12:57
16:22:57
16:38:34
16:55:45
17:11:25
17:21:25
14:05:45
14:19:35
14:29:35
14:44:00
14:59:38
15:09:38
17/08/2017
22/08/2017
25/08/2017
28/08/2017
30/08/2017
Date / Hour

Figure 10